

Triple- α reaction rates below $T_9 = 3$ by a non-adiabatic three-body model

M. Katsuma^{a,b}

^a*Institut d'Astronomie et d'Astrophysique, Université Libre de Bruxelles, Brussels B-1050, Belgium*

^b*Advanced Mathematical Institute, Osaka City University, Osaka 558-8585, Japan*

Abstract

The triple- α reaction from ternary continuum states at off-resonant energies, $\alpha + \alpha + \alpha \rightarrow {}^{12}\text{C}$, still remains in unsolved problems. This direct process is estimated with a non-adiabatic Faddeev hyper-spherical harmonics and R -matrix expansion method. After reviewing this model, the resultant photo-disintegration of ${}^{12}\text{C}(2_1^+ \rightarrow 0^+)$ is shown to be in 10^{-15} – 10^{-3} pico-barn order for $0.15 \leq E \leq 0.35$ MeV. This is far below the values predicted by the recent adiabatic calculations. In spite of the large difference, the derived reaction rates are illustrated to be concordant with the current evaluated rates for $0.08 \leq T_9 \leq 3$ including helium burning temperatures. The difference below $E = 0.20$ MeV can be seen in the rates for $T_9 \leq 0.07$. In comparison with the calculations, the triple- α reaction rates are found to be reduced by about 10^{-4} at $T_9 = 0.05$, because of an accurate description for ${}^8\text{Be}$ break-up. Uncertainties of the rates are also estimated by examining sensitivity to 3α potentials. With introducing three-body S -factors and a resonant term, the present rates are expressed in an analytic form, and they are provided in a tabular form for astrophysical applications. To update the evaluated rates, non-resonant sequential process between $\alpha + {}^8\text{Be}$ may be eliminated by hand.

Keywords: Triple- α reaction rates, Three-body model, Helium burning

Email address: mkatsuma@gmail.com (M. Katsuma)

1. Introduction

The triple- α reaction plays a crucial role in stellar evolution and concomitant nucleosynthesis [1, 2]. This reaction, followed by $^{12}\text{C}(\alpha,\gamma)^{16}\text{O}$ [3], controls C/O ratio at the end of helium burning phase in stars, which decides a fate of massive stars up to their supernova explosion. In contrast to $^{12}\text{C}(\alpha,\gamma)^{16}\text{O}$, the triple- α reaction is currently well-understood through the experimental studies of the 0_2^+ state in ^{12}C ($E = 0.379$ MeV), *e.g.* [4–6], *i.e.*, the triple- α reaction rates at helium burning temperatures, $T_9 > 0.1$, have been determined well with the sequential process via the narrow resonances: $\alpha + \alpha \rightarrow {}^8\text{Be}(0_1^+)$; $\alpha + {}^8\text{Be} \rightarrow {}^{12}\text{C}(0_2^+)$ [4, 7]. T_9 is temperature in the unit of 10^9 K; E is the center-of-mass energy to the 3α threshold in ^{12}C .

Apart from the sequential process, the triple- α reaction from ternary continuum states is referred to as the direct triple- α process: $\alpha + \alpha + \alpha \rightarrow {}^{12}\text{C}$. This process is generally expected to be very slow, because three α -particles almost simultaneously collide and fuse into a ^{12}C nucleus. Thus, it is neglected or is treated in some approximations. In NACRE [4], ${}^8\text{Be}$ is assumed to be bound as a particle, and the reaction rates have been estimated by an improved model based on the pioneering works of [8, 9]. To ponder 3α continuum states more theoretically, formulae in hyper-spherical coordinates have been adopted in *e.g.* [10], and recently, the Coulomb modified Faddeev (CMF) method [11–13] and adiabatic channel function (ACF) expansion method [14] may have achieved the successful progress quantitatively. However, the direct triple- α process, which may dominate the rates at low temperatures ($T_9 < 0.1$), still seems to remain in an open question.

CMF and ACF postulate adiabatic conditions by using cutoff procedure [11] and adiabatic channel functions [14]. “Adiabatic” means an approximation with a difference of velocity among α -particles. Let me consider $a + A(b + c)$ scattering for example. a , b , c are particles. A consists of b and c . Here, I assume that the relative motion between $b + c$ is very slow, compared with the velocity between $a + A$. In this situation, incoming- a can see a pair of $b + c$ keeping their distance, and scattering amplitudes are described separably with a fixed distance of the pair. The final cross sections are obtained by integrating the components over the distance. The adiabatic feature is constructed under the constrained coordinates [15, 16]. In ACF, hyperradial motion, variation in the global size, is assumed to be slow. However, for the triple- α reaction, the relative motion among α -particles ought to vary more flexibly during the collision. Therefore, theoretical challenges

would have to be made to describe the ternary continuum more rigorously.

When seeing the calculated photo-disintegration cross sections of $^{12}\text{C}(2_1^+ \rightarrow 0^+)$ in Fig. 4 of [14], you could find the large discrepancy from the one currently considered. As a non-adiabatic model, Ref. [17, 18] adopts a Faddeev hyper-spherical harmonics and R -matrix (HHR) expansion method. HHR is based on R -matrix theory [19], describing the 3α bound and continuum states quantum-mechanically. Although HHR makes the large difference in the rates at low temperatures, the derived rates are consistent with the NACRE rates above $T_9 = 0.07$, *i.e.*, the cross sections within the Gamow energy-window [4], $E > 0.20$ MeV, may have some reasonable values. Then, what is the difference between the calculated cross sections at off-resonant energies?

In the present article, I discuss the direct triple- α process and derived reaction rates by using a non-adiabatic Faddeev HHR expansion method [16–18, 20–22]. I illustrate the calculated photo-disintegration cross sections of $^{12}\text{C}(2_1^+ \rightarrow 0^+)$. At the same time, I discuss the difference between adiabatic and non-adiabatic approaches. The derived rates are expressed in an analytic form, and they are listed in a numerical table for astrophysical applications. They are also converted into REACLIB format [23]. I show that the current evaluated rates are reduced by about 10^{-4} at $T_9 = 0.05$, because of an accurate description for ^8Be break-up. In addition, I estimate uncertainties of the rates by examining sensitivity to 3α potentials. Before discussing my calculated results, I first review HHR, and I describe a formula of reaction rates with introducing a three-body type of S -factors. And then, I describe basic interaction and related density distribution of the states in ^{12}C . The calculated results shown here are independent of the precedent study with HHR [17, 18]. To avoid confusion, my calculation is referred to as HHR*.

This article consists of six sections. In the following section, I review the Faddeev HHR* expansion method used in the present study. In §3, I describe a formula of reaction rates for the triple- α reaction. The interaction potentials for $\alpha+\alpha$ and 3α are examined, and the density distribution functions of the states in ^{12}C are illustrated in §4. The calculated triple- α reaction rates are discussed in §5. The derived reaction rates are expressed in an analytic form, and they are also provided in a tabular form. The summary is in §6.

2. Non-adiabatic Faddeev HHR* expansion

In this section, I first introduce the three-body Schrödinger equation and define basis functions in hyper-spherical coordinates, and then, I expound

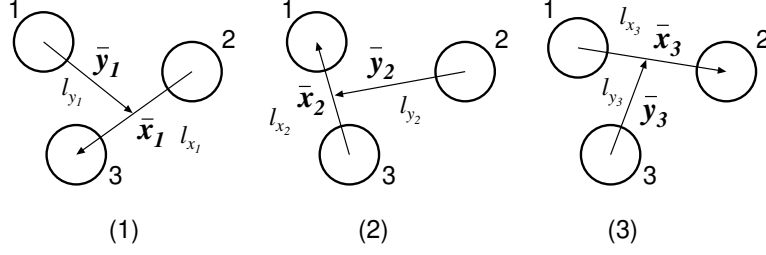


Figure 1: Jacobi coordinates, used in the present article.

3α symmetrization, and describe coupling potentials in the derived coupled-channel (CC) equations. After recalling eigenvalue equations, I review the R -matrix expansion method for 3α continuum states. Finally, I explain R -matrix propagation for numerical solutions in the external region.

2.1. Faddeev hyper-spherical harmonics (HH) expansion

The triple- α system satisfies the three-body Schrödinger equation,

$$(\hat{H}_{3\alpha} - E)\Psi = 0. \quad (1)$$

$\hat{H}_{3\alpha}$ is three-body Hamiltonian, $\hat{H}_{3\alpha} = \hat{T} + \hat{V}_{12} + \hat{V}_{23} + \hat{V}_{31} + \hat{V}_{3\alpha}$. \hat{T} is the kinetic energy operator. \hat{V}_{ij} is interaction between two α -particles, and $\hat{V}_{3\alpha}$ is 3α interaction. This equation is expressed as the so-called Faddeev equations, consisting of three components:

$$\begin{cases} (\hat{T}_{(1)} + \hat{V}_{23} + \hat{V}_{3\alpha} - E)\Psi_{(1)} = -\hat{V}_{23}\Psi_{(2)} - \hat{V}_{23}\Psi_{(3)} \\ (\hat{T}_{(2)} + \hat{V}_{31} + \hat{V}_{3\alpha} - E)\Psi_{(2)} = -\hat{V}_{31}\Psi_{(3)} - \hat{V}_{31}\Psi_{(1)} \\ (\hat{T}_{(3)} + \hat{V}_{12} + \hat{V}_{3\alpha} - E)\Psi_{(3)} = -\hat{V}_{12}\Psi_{(1)} - \hat{V}_{12}\Psi_{(2)} \end{cases} \quad (2)$$

The total wavefunction is a sum of the components, $\Psi = \Psi_{(1)} + \Psi_{(2)} + \Psi_{(3)}$. Jacobi coordinates ($\bar{\mathbf{x}}_i$, $\bar{\mathbf{y}}_i$) are defined as y-type ($i = 1, 2$) and T-type ($i = 3$) in Fig. 1. Due to the symmetric 3α system, the coupled-equations of Eq. (2) are reduced to the single component with the sum of three pairwise interaction and 3α force, $(\hat{T}_{(3)} + \hat{V} - E)\Psi_{(3)} = 0$, as described at the end of this subsection. Let me rewrite the third component in

$$\left(-\frac{\hbar^2}{2\mu_{12}} \nabla_{\bar{\mathbf{x}}_3}^2 - \frac{\hbar^2}{2\mu_{(12)3}} \nabla_{\bar{\mathbf{y}}_3}^2 + \hat{V} \right) \Psi_{lm} = E \Psi_{lm}, \quad (3)$$

$$\hat{V} = \sum_{i<j}^3 \hat{V}_{ij} + \hat{V}_{3\alpha}. \quad (4)$$

l is spin of the states in ^{12}C . m is the projection of l . μ_{12} and $\mu_{(12)3}$ are the reduced mass for $\alpha+\alpha$ and $\alpha+^8\text{Be}$. If Jacobi coordinates are scaled as $\mathbf{x}_3 \equiv \sqrt{\mu_{12}/m_N} \bar{\mathbf{x}}_3$ and $\mathbf{y}_3 \equiv \sqrt{\mu_{(12)3}/m_N} \bar{\mathbf{y}}_3$, Eq. (3) becomes

$$\left[-\frac{\hbar^2}{2m_N} (\nabla_{x_i}^2 + \nabla_{y_i}^2) + \hat{V} \right] \Psi_{lm} = E \Psi_{lm}, \quad (5)$$

where m_N is nucleon mass. From the scaled Jacobi coordinates, the hyper-spherical coordinates $(\rho, \theta_i, \hat{\mathbf{x}}_i, \hat{\mathbf{y}}_i)$ are defined by

$$\rho^2 = x_i^2 + y_i^2, \quad (6)$$

$$\theta_i = \arctan\left(\frac{x_i}{y_i}\right). \quad (7)$$

ρ and θ_i are the hyper-radius and hyper-angle, respectively. (*e.g.* [16]) When Ψ_{lm} is separated into the hyper-radial part and hyper-angle part (as Eq. (12)), Eq. (5) is transformed into a similar form of ordinary CC equations with $L = K + 3/2$ for inelastic scattering (*e.g.* [15, 24]),

$$[T_\gamma + U_{\gamma'\gamma}^l(\rho) - \epsilon] \chi_\gamma^l(\rho) = - \sum_{\gamma' \neq \gamma} U_{\gamma'\gamma}^l(\rho) \chi_{\gamma'}^l(\rho), \quad (8)$$

where

$$T_\gamma = \frac{d^2}{d\rho^2} - \frac{(K + 3/2)(K + 5/2)}{\rho^2}, \quad (9)$$

$$U_{\gamma'\gamma}^l(\rho) = -\frac{2m_N}{\hbar^2} V_{\gamma'\gamma}^l(\rho), \quad (10)$$

$$\epsilon = -\frac{2m_N}{\hbar^2} E. \quad (11)$$

$\chi_\gamma^l(\rho)$ are hyper-radial wavefunctions. The hyper-angle part is solved with Jacobi polynomials. $V_{\gamma'\gamma}^l$ are coupling potentials. K are hyper-angular momenta. γ is a label of channels, $\gamma = (K, l_{x_3}, l_{y_3})$. l_{x_3} and l_{y_3} are internal angular momenta in Jacobi coordinates. l_{x_3} is only even. This condition of the partial wave ensures the symmetrization of the system. l_{y_3} is also even for 0^+ and 2^+ , because the parity of the 3α system is given by $\pi = (-)^l = (-)^{l_{x_3} + l_{y_3}}$. The $K = 2$ channel for 0^+ is vanished due to the symmetric 3α system.

The basis functions are defined by

$$\Psi_{lm} = \rho^{-5/2} \sum_{\gamma} \chi_\gamma^l(\rho) \Phi_{lm}^\gamma(\Omega_5^{(3)}), \quad (12)$$

$$\chi_\gamma^l(\rho) = \sum_n \bar{c}_\gamma^n w_n^\gamma(\rho), \quad (13)$$

where $\Omega_5^{(3)} \equiv (\theta_3, \hat{\mathbf{x}}_3, \hat{\mathbf{y}}_3)$. n is the number of radial nodes ($n = 0, 1, \dots$). K in γ runs up to $K = 26$ for 0^+ [18] and $K = 12$ for 2^+ [18]. The internal angular momenta up to $l_{x_3} = 12$ and $l_{y_3} = 12$ are taken into account. \bar{c}_γ^n are the coefficients of expansion. $w_n^\gamma(\rho)$ are eigenfunctions, satisfying the following equation with eigen-energies $\epsilon_{n\gamma}$:

$$[T_\gamma + U_{\gamma\gamma}^l(\rho) - \epsilon_{n\gamma}] w_n^\gamma(\rho) = 0. \quad (14)$$

$w_n^\gamma(\rho)$ are assumed to have a fixed logarithmic derivative $b_c \equiv d \ln w_n^\gamma(\rho) / d\rho = 0$ at $\rho = a_c$, *i.e.*, they ensure that the $b_c = 0$ formula of R -matrix theory [16, 19, 22] can be used. The hyper-harmonic functions are defined by

$$\Phi_{lm}^\gamma(\Omega_5^{(3)}) = \phi_K^{l_{x_3} l_{y_3}}(\theta_3) [\mathcal{Y}_{l_{x_3}}(\hat{\mathbf{x}}_3) \otimes \mathcal{Y}_{l_{y_3}}(\hat{\mathbf{y}}_3)]_{lm}, \quad (15)$$

where $\mathcal{Y}_{lm} \equiv i^l Y_{lm}$. Y_{lm} are spherical harmonics. $\phi_K^{l_x l_y}$ are defined by

$$\phi_K^{l_{x_3} l_{y_3}}(\theta_3) = N_{n_\theta}^{l_{x_3} l_{y_3}} (\sin \theta_3)^{l_{x_3}} (\cos \theta_3)^{l_{y_3}} \mathcal{G}_{n_\theta}(n_a, n_b; \sin^2 \theta_3), \quad (16)$$

$$N_{n_\theta}^{l_{x_3} l_{y_3}} = \left[\frac{2(n_a + 2n_\theta) \Gamma(n_a + n_\theta) \Gamma(n_b + n_\theta)}{n_\theta! \Gamma(n_\theta + l_{y_3} + 3/2)} \right]^{\frac{1}{2}} \frac{1}{\Gamma(n_b)}. \quad (17)$$

\mathcal{G}_{n_θ} are Jacobi polynomials, $n_\theta = \frac{1}{2}(K - l_{x_3} - l_{y_3})$, $n_a = l_{x_3} + l_{y_3} + 2$, $n_b = l_{x_3} + 3/2$. Γ are gamma functions. The values of K are only even, because $(l_{x_3} + l_{y_3})$ are even. $\Phi_{lm}^\gamma(\Omega_5^{(3)})$ are independent of ρ , and they are different from the adiabatic channel functions in [14]. The basis functions satisfy the following orthogonal conditions in a box with the finite interval:

$$\int_0^{a_c} w_{n'}^\gamma(\rho) w_n^\gamma(\rho) d\rho = \delta_{n'n}, \quad (18)$$

$$\int \Phi_{l'm'}^{\gamma'*}(\Omega_5^{(3)}) \Phi_{lm}^\gamma(\Omega_5^{(3)}) d\Omega_5^{(3)} = \delta_{\gamma'\gamma} \delta_{l'l} \delta_{m'm}. \quad (19)$$

$\Phi_{lm}^\gamma(\Omega_5^{(3)})$ are expanded by the hyper-harmonic functions in the y-type coordinates of Fig. 1, as follows:

$$\Phi_{lm}^{K l_{x_3} l_{y_3}}(\Omega_5^{(3)}) = \sum_{l_{x_i} l_{y_i}} \langle l_{x_i} l_{y_i} | l_{x_3} l_{y_3} \rangle_{Kl} \Phi_{lm}^{K l_{x_i} l_{y_i}}(\Omega_5^{(i)}), \quad (20)$$

where $\langle l_{x_i} l_{y_i} | l_{x_3} l_{y_3} \rangle_{Kl}$ are the Raynal-Revai (RR) coefficients [25]. K, l, m are conserved in this unitary transformation. The RR coefficients are used for convenience when nuclear potentials depend on l_{x_i} (Eq. (36)).

$w_n^\gamma(\rho)$ are expanded by a set of arbitrary orthonormal functions $\varphi_{n'}^K(\rho)$, as follows:

$$w_n^\gamma(\rho) = \sum_{n'=0}^{n_\rho-1} d_{\gamma n'}^{n'} \varphi_{n'}^K(\rho), \quad (21)$$

where $d_{\gamma n'}^{n'}$ are the coefficients of expansion. $(n_\rho - 1)$ is the maximum number of radial nodes. If the coefficients are rewritten as $c_\gamma^{n'} = \sum_n \bar{c}_\gamma^n d_{\gamma n}^{n'}$, $w_n^\gamma(\rho)$ in the formula can be replaced with $\varphi_n^K(\rho)$.

The wavefunctions in Eqs. (3) and (8) are therefore expanded as

$$\Psi_{lm} = \rho^{-5/2} \sum_{\gamma n} c_\gamma^n \varphi_n^K(\rho) \Phi_{lm}^\gamma(\Omega_5^{(3)}), \quad (22)$$

$$\chi_\gamma^l(\rho) = \sum_{n=0}^{n_\rho-1} c_\gamma^n \varphi_n^K(\rho). \quad (23)$$

Ψ_{lm} is normalized as

$$\int |\Psi_{lm}|^2 \rho^5 d\rho d\Omega_5^{(3)} = \int |\Psi_{lm}|^2 d\mathbf{x}_3 d\mathbf{y}_3 = \mathcal{J}^3 \int |\Psi_{lm}|^2 d\bar{\mathbf{x}}_3 d\bar{\mathbf{y}}_3 = 1, \quad (24)$$

where $\mathcal{J} = \sqrt{\mu_{12}\mu_{(12)3}/m_N^2} = 4/\sqrt{3}$. If a large number of basis functions are used in calculations, the final results are independent of a choice of $\varphi_n^K(\rho)$.

In HHR*, the harmonic oscillator wavefunctions in hyper-spherical coordinates are adopted as the orthonormal functions,

$$\varphi_n^K(\rho) = \left[\frac{2\nu n!}{(n+K+2)!} \right]^{\frac{1}{2}} (\nu\rho)^{K+\frac{5}{2}} \exp\left(-\frac{1}{2}(\nu\rho)^2\right) L_n^{(K+2)}((\nu\rho)^2), \quad (25)$$

where $L_n^{(K+2)}$ are associated Laguerre polynomials. ν is a harmonic oscillator range. $\nu = 0.23 \text{ fm}^{-1}$ and $n_\rho = 160$ are used to make expansion efficiently. The derivatives of Eq. (25) are

$$\frac{d\varphi_n^K(\rho)}{d\rho} = \frac{1}{\rho} \left[\left(K + \frac{5}{2} + 2n - (\nu\rho)^2 \right) \varphi_n^K(\rho) - 2\sqrt{n(n+K+2)} \varphi_{n-1}^K(\rho) \right]. \quad (26)$$

In the last part of this subsection, I describe the symmetric properties of the 3α wavefunction [16–18]. With respect to the exchange of α -particles $1 \leftrightarrow 2$, $\Psi_{(1)}$ has a relation as

$$\hat{\mathcal{P}}_{12} \Psi_{(1)} = \Psi_{(2)} = (-)^{l_{x_1}} \Psi_{(1)}, \quad (27)$$

where $\hat{\mathcal{P}}_{ij}$ is the exchange operator between two α -particles. The phase comes out from $\mathcal{Y}_{l_{x_i}}(-\hat{\mathbf{x}}_i) = (-)^{l_{x_i}} \mathcal{Y}_{l_{x_i}}(\hat{\mathbf{x}}_i)$ in Eq. (15). $\Psi_{(2)}$ and $\Psi_{(3)}$ have

$$\begin{aligned}\hat{\mathcal{P}}_{12}\Psi_{(2)} &= \Psi_{(1)} = (-)^{l_{x_2}}\Psi_{(2)}, \\ \hat{\mathcal{P}}_{12}\Psi_{(3)} &= \Psi'_{(3)} = (-)^{l_{x_3}}\Psi_{(3)}.\end{aligned}\quad (28)$$

Likewise, $2 \leftrightarrow 3$:

$$\begin{aligned}\hat{\mathcal{P}}_{23}\Psi_{(1)} &= \Psi'_{(1)} = (-)^{l_{x_1}}\Psi_{(1)}, \\ \hat{\mathcal{P}}_{23}\Psi_{(2)} &= \Psi_{(3)} = (-)^{l_{x_2}}\Psi_{(2)}, \\ \hat{\mathcal{P}}_{23}\Psi_{(3)} &= \Psi_{(2)} = (-)^{l_{x_3}}\Psi_{(3)}.\end{aligned}\quad (29)$$

$3 \leftrightarrow 1$:

$$\begin{aligned}\hat{\mathcal{P}}_{31}\Psi_{(1)} &= \Psi_{(3)} = (-)^{l_{x_1}}\Psi_{(1)}, \\ \hat{\mathcal{P}}_{31}\Psi_{(2)} &= \Psi'_{(2)} = (-)^{l_{x_2}}\Psi_{(2)}, \\ \hat{\mathcal{P}}_{31}\Psi_{(3)} &= \Psi_{(1)} = (-)^{l_{x_3}}\Psi_{(3)}.\end{aligned}\quad (30)$$

Therefore, the exchange between any pair of α -particles to the total wave-functions is obtained as

$$\hat{\mathcal{P}}\Psi = (-)^{l_{x_1}}\Psi_{(1)} + (-)^{l_{x_2}}\Psi_{(2)} + (-)^{l_{x_3}}\Psi_{(3)}, \quad (31)$$

where $\hat{\mathcal{P}} = (\hat{\mathcal{P}}_{12} + \hat{\mathcal{P}}_{23} + \hat{\mathcal{P}}_{31})/3$. If l_{x_1} , l_{x_2} , and l_{x_3} are even, I find

$$\hat{\mathcal{P}}\Psi = \Psi. \quad (32)$$

Under this constraint on the partial waves, the right hand of the first component of Eq. (2) becomes

$$\hat{V}_{23}\Psi_{(2)} = \hat{V}_{31}\Psi_{(1)}, \quad (33)$$

$$\hat{V}_{23}\Psi_{(3)} = \hat{V}_{12}\Psi_{(1)}. \quad (34)$$

The exchange of $1 \leftrightarrow 2$ ($3 \leftrightarrow 1$) is used in Eq. (33) (Eq. (34)). Thus, the first component of Eq. (2) is rewritten as

$$[\hat{T}_{(1)} + (\hat{V}_{12} + \hat{V}_{23} + \hat{V}_{31}) + \hat{V}_{3\alpha} - E] \Psi_{(1)} = 0. \quad (35)$$

The same transformation can be performed on the second and third Faddeev components. Consequently, three sets of the independent CC equations are obtained in the same expression. In other words, this 3α symmetrization efficiently reduces the number of channels included in Eq. (2).

2.2. Coupling potentials

The coupling potentials in Eq. (10) are given in

$$\begin{aligned}
V_{\gamma'\gamma}^l(\rho) &= \int \Phi_{lm}^{\gamma'*}(\Omega_5^{(3)}) \hat{V} \Phi_{lm}^{\gamma}(\Omega_5^{(3)}) d\Omega_5^{(3)} \\
&= V_{3\alpha}^l(\rho) \delta_{\gamma'\gamma} + \delta_{l'_{x_3} l_{x_3}} \delta_{l'_{y_3} l_{y_3}} F_{K'K}^{l_{x_3} l_{y_3}}(\rho) \\
&+ \sum_{l_{x_1} l_{y_1}} \langle l_{x_1} l_{y_1} | l'_{x_3} l'_{y_3} \rangle_{K'l} \langle l_{x_1} l_{y_1} | l_{x_3} l_{y_3} \rangle_{Kl} F_{K'K}^{l_{x_1} l_{y_1}}(\rho) \\
&+ \sum_{l_{x_2} l_{y_2}} \langle l_{x_2} l_{y_2} | l'_{x_3} l'_{y_3} \rangle_{K'l} \langle l_{x_2} l_{y_2} | l_{x_3} l_{y_3} \rangle_{Kl} F_{K'K}^{l_{x_2} l_{y_2}}(\rho), \quad (36)
\end{aligned}$$

where

$$F_{K'K}^{l_{x_i} l_{y_i}}(\rho) = \int \phi_{K'}^{l_{x_i} l_{y_i}}(\theta_i) V_{2\alpha}^{l_{x_i}}(\bar{x}_i) \phi_K^{l_{x_i} l_{y_i}}(\theta_i) \cos^2 \theta_i \sin^2 \theta_i d\theta_i. \quad (37)$$

$V_{2\alpha}^{l_{x_i}}$ and $V_{3\alpha}^l$ are $\alpha+\alpha$ and 3α interaction potentials, respectively. $V_{2\alpha}^{l_{x_i}}$ consists of two parts, nuclear and Coulomb potentials, $V_{2\alpha}^{l_{x_i}} = V_N^{l_{x_i}} + V_C$.

Both diagonal and non-diagonal components of Eq. (36) vary as $Z_{\gamma'\gamma}^l e^2/\rho$ in the asymptotic region [18, 21, 26]. In HHR*, $Z_{\gamma'\gamma}^l$ are given as

$$\begin{aligned}
Z_{\gamma'\gamma}^l &= 4\sqrt{2} \left(\delta_{l'_{x_3} l_{x_3}} \delta_{l'_{y_3} l_{y_3}} F_{(C)K'K}^{l_{x_3} l_{y_3}} \right. \\
&+ \sum_{l_{x_1} l_{y_1}} \langle l_{x_1} l_{y_1} | l'_{x_3} l'_{y_3} \rangle_{K'l} \langle l_{x_1} l_{y_1} | l_{x_3} l_{y_3} \rangle_{Kl} F_{(C)K'K}^{l_{x_1} l_{y_1}} \\
&+ \left. \sum_{l_{x_2} l_{y_2}} \langle l_{x_2} l_{y_2} | l'_{x_3} l'_{y_3} \rangle_{K'l} \langle l_{x_2} l_{y_2} | l_{x_3} l_{y_3} \rangle_{Kl} F_{(C)K'K}^{l_{x_2} l_{y_2}} \right), \\
&= 4\sqrt{2} \left(\delta_{l'_{x_3} l_{x_3}} \delta_{l'_{y_3} l_{y_3}} F_{(C)K'K}^{l_{x_3} l_{y_3}} + \sum_t \mathcal{I}_{l_{x_3} l_{y_3}}^{l'_{y_3} l'_{x_3}} \right. \\
&\cdot \left. \int \phi_{K'}^{l'_{x_3} l'_{y_3}}(\theta_3) \bar{f}_t(\theta_3) \phi_K^{l_{x_3} l_{y_3}}(\theta_3) \cos^2 \theta_3 \sin^2 \theta_3 d\theta_3 \right), \quad (38)
\end{aligned}$$

where

$$\begin{aligned}
F_{(C)K'K}^{l_{x_i} l_{y_i}} &= \int \phi_{K'}^{l_{x_i} l_{y_i}}(\theta_i) \frac{1}{\sin \theta_i} \phi_K^{l_{x_i} l_{y_i}}(\theta_i) \cos^2 \theta_i \sin^2 \theta_i d\theta_i, \quad (39) \\
\mathcal{I}_{l_{x_3} l_{y_3}}^{l'_{y_3} l'_{x_3}} &= i^{(l_{x_3} - l'_{x_3} + t) + (l_{y_3} - l'_{y_3} + t)} (-)^l \hat{l}_{x_3}^l \hat{l}_{y_3}^l \hat{l}_{x_3}^l \hat{l}_{y_3}^l (2t + 1)
\end{aligned}$$

$$\cdot \begin{pmatrix} l'_{x3} & t & l_{x3} \\ 0 & 0 & 0 \end{pmatrix} \begin{pmatrix} l'_{y3} & t & l_{y3} \\ 0 & 0 & 0 \end{pmatrix} \left\{ \begin{matrix} l & l'_{y3} & l'_{x3} \\ t & l_{x3} & l_{y3} \end{matrix} \right\}, \quad (40)$$

$$\bar{f}_t(\theta_3) = \int_{-1}^1 \frac{P_t(z) dz}{\sqrt{\xi_x^2 + \xi_y^2 + 2\xi_x \xi_y z}}, \quad (41)$$

$\xi_x = (1/2) \sin \theta_3$, $\xi_y = (\sqrt{3}/2) \cos \theta_3$, $\hat{l} = \sqrt{2l+1}$. P_t are Legendre polynomials. t is only even. $(:::)$ and $\{:::\}$ are 3-J and 6-J symbols, respectively. The Sommerfeld parameter of the γ channel is defined as $\eta_\gamma \equiv Z_{\gamma\gamma}^l e^2 / (\hbar v)$, $v = \sqrt{2E/m_N}$.

2.3. Solving hyper-radial equations in the interior region

The CC equations of Eq. (8) are expressed by eigenvalue equations as

$$(\mathbf{T} + \mathbf{U})\mathbf{X} = \epsilon\mathbf{X}. \quad (42)$$

\mathbf{T} and \mathbf{U} are $(n_\gamma n_\rho) \times (n_\gamma n_\rho)$ matrices of the kinetic energy operator and interaction. n_γ is the number of channels. \mathbf{X} is a coefficient vector with $(n_\gamma n_\rho)$ components. The matrix elements of \mathbf{T} and \mathbf{U} are given in

$$\langle \varphi_{n'}^K | T_\gamma | \varphi_n^K \rangle = \begin{cases} -\sqrt{n(n+K+2)} \nu^2 & n' = n-1 \\ -(2n+K+3) \nu^2 & n' = n \\ -\sqrt{(n+1)(n+K+3)} \nu^2 & n' = n+1 \\ 0 & \text{others} \end{cases} \quad (43)$$

$$\langle \varphi_{n'}^{K'} | U_{\gamma'\gamma}^l | \varphi_n^K \rangle = \int_0^{a_c} \varphi_{n'}^{K'}(\rho) U_{\gamma'\gamma}^l(\rho) \varphi_n^K(\rho) d\rho. \quad (44)$$

Equation (42) is solved with matrix diagonalization for $\mathbf{H} = \mathbf{T} + \mathbf{U}$:

$${}^t\mathbf{W}\mathbf{H}\mathbf{W} = \begin{pmatrix} \epsilon_1 & 0 & \dots & 0 \\ 0 & \epsilon_2 & \dots & 0 \\ \vdots & \vdots & \ddots & \vdots \\ 0 & 0 & \dots & \epsilon_{(n_\gamma n_\rho)} \end{pmatrix}, \quad (45)$$

$$\mathbf{W} = (\mathbf{X}_1, \mathbf{X}_2, \dots, \mathbf{X}_{(n_\gamma n_\rho)}). \quad (46)$$

\mathbf{W} is a unitary matrix. The linearly-independent solutions are expressed with ϵ_i and \mathbf{X}_i . The eigen-energies are given by

$$\tilde{E}(l_i^\pi) = -\frac{\hbar^2}{2m_N}\epsilon_i. \quad (47)$$

i is a label of the states, given in order of the excitation energy. $i = 1$ means the lowest energy of states with l^π . $\tilde{E}(0_2^+)$ is equivalent to the formal energy of 0_2^+ in R -matrix theory [19]. It is however considered as the observed energy $E(0_2^+)$, because width is very narrow. $\tilde{E}(l_1^+)$ for 0_1^+ and 2_1^+ are also observables, $\tilde{E}(l_1^+) = E(l_1^+)$. The corresponding eigenfunctions are

$$\Psi_{i,lm} = \rho^{-5/2} \sum_{\gamma n} c_{\gamma i}^n \varphi_n^K(\rho) \Phi_{lm}^\gamma(\Omega_5^{(3)}), \quad (48)$$

$$\chi_{\gamma i}^l(\rho) = \sum_{n=0}^{n_\rho-1} c_{\gamma i}^n \varphi_n^K(\rho). \quad (49)$$

For $E(l_i^\pi) < 0$, $\chi_{\gamma i}^l(\rho)$ are bound state wavefunctions, extrapolated as

$$\chi_{\gamma i}^l(\rho) \rightarrow \tilde{\mathcal{N}}_{\gamma i}^l W_{-\eta_\gamma, K+2}(2\kappa\rho), \quad (50)$$

where $\kappa = \sqrt{\epsilon_i}$; $W_{-\eta_\gamma, K+2}$ are Whittaker functions; $\tilde{\mathcal{N}}_{\gamma i}^l$ are normalization constants. The tail of 2_1^+ is extrapolated with Eq. (50). For $E(l_i^\pi) > 0$, $\chi_{\gamma i}^l(\rho)$ are resonant state wavefunctions. If resonant states exist experimentally in low-lying levels, the calculated eigenstates may correspond to the experimental levels. However, most of the eigenstates are mathematically orthogonal states that do not have any specific features in physics. The continuum states with the scattering boundary condition are expressed by a linear-combination of the eigenfunctions. I describe it in §2.4.

To understand nuclear structure of the generated eigenstates, density distribution functions are defined by

$$\mathcal{P}_{l_i^\pi}(\bar{x}_3, \bar{y}_3) \equiv \mathcal{J}^3 \bar{x}_3^2 \bar{y}_3^2 \int |\Psi_{i,lm}|^2 d\hat{\mathbf{x}}_3 d\hat{\mathbf{y}}_3. \quad (51)$$

The density is normalized as $\int \mathcal{P}_{l_i^\pi}(\bar{x}_3, \bar{y}_3) d\bar{x}_3 d\bar{y}_3 = 1$. The reduced width amplitude for $\alpha+{}^8\text{Be}$ in 0_2^+ is defined as

$$\tilde{\gamma}_{\alpha+{}^8\text{Be}}(\bar{y}_3) \equiv \sqrt{\frac{\mathcal{J}^3 \hbar^2}{2\mu_{(12)3} \bar{y}_3}} \int \Psi_{s\text{Be}}(\bar{\mathbf{x}}_3) \Psi_{2,00}(\bar{\mathbf{x}}_3, \bar{\mathbf{y}}_3) d\bar{\mathbf{x}}_3 d\hat{\mathbf{y}}_3. \quad (52)$$

$\Psi_{8\text{Be}}$ is the wavefunction of ${}^8\text{Be}(0_1^+)$. The $\alpha+{}^8\text{Be}$ width is given as

$$\Gamma_{\alpha+8\text{Be}}(\bar{y}_3) = 2\tilde{\gamma}_{\alpha+8\text{Be}}^2(\bar{y}_3)P_{\alpha,0}(\bar{y}_3), \quad (53)$$

where $P_{\alpha,0}$ is the penetration factor, calculated from Coulomb wavefunctions (*e.g.* [16, 19, 22]). The α -decay width of ${}^{12}\text{C}(0_2^+)$ is calculated from $\Gamma(0_2^+) = 3 \times \Gamma_{\alpha+8\text{Be}}$ in the present article. The dimensionless reduced width is

$$\theta_{\alpha+8\text{Be}}^2(\bar{y}_3) = \tilde{\gamma}_{\alpha+8\text{Be}}^2(\bar{y}_3)/\gamma_W^2, \quad (54)$$

$\gamma_W^2 = 3\hbar^2/(2\mu_{(12)3}\bar{y}_3^2)$. The root-mean-square (rms) radius is given by

$$R_{\text{rms}}(l_i^\pi) = \sqrt{\langle r_\alpha^2 \rangle + \frac{1}{12} \sum_\gamma \int |\chi_{\gamma i}^l(\rho)|^2 \rho^2 d\rho}, \quad (55)$$

where $\langle r_\alpha^2 \rangle^{1/2} = 1.4735$ fm (§4.1). The monopole matrix element [10, 14] between 0_2^+ and 0_1^+ is defined as

$$M(E0; 0_2^+ \rightarrow 0_1^+) = \frac{e}{2} \sum_\gamma \int \chi_{\gamma 2}^{0+}(\rho) \chi_{\gamma 1}^{0+}(\rho) \rho^2 d\rho. \quad (56)$$

The internal structure of the bound 2_1^+ state may not be described by a pure 3α component [14], and the actual wavefunction is assumed to be replaced with

$$\Psi_{2_1^+} = \mathcal{N}\Psi_{1,2m}. \quad (57)$$

As assumed in HHR, CMF, and ACF, the resultant transition strength is given by multiplying the calculated one by a factor of \mathcal{N}^2 . In HHR*, \mathcal{N}^2 is obtained by normalizing the calculated γ width of 0_2^+ to 3.9 ± 0.39 meV [27].

2.4. *R-matrix expansion*

R-matrix theory was developed by [19], and it has been widely used to evaluate the experimental data phenomenologically. In a basic idea of theory, low-energy nuclear reactions are assumed to occur at a surface of nuclei after penetrating the effective barrier made by nuclear, Coulomb, and centrifugal potentials. The barrier is approximately located at the reach of nuclear force between colliding nuclei, and its position is defined as a channel radius $\rho = a_c$. A compound nucleus is assumed to be formed in a sphere with the radius a_c ,

and the wavefunction connects to all possible reaction channels at $\rho = a_c$. In the phenomenological evaluation of nuclear data, probabilities to the respective reaction channels are parameterized as the resonance energies and widths. As a consequence, the resonant states in the interior region do not need to be solved microscopically. In the external region, the wavefunctions are given by Coulomb wavefunctions, because nuclear interaction is negligible. Recently, this method has been referred to as the *phenomenological R-matrix method* [28].

On the other hand, internal nuclear structure is assumed to be expanded by a set of arbitrary orthonormal basis in *R-matrix theory*. Accordingly, internal wavefunctions are calculated microscopically in model Hamiltonian. Resonance, transition probability, and reaction rates are derived from them on the theoretical footing. This microscopic approach is referred to as the *calculable R-matrix method* [28]. HHR* is classified into the latter. The final result is independent of a_c if many basis functions are used. In this method, a_c is set for convenience, and it appears to be different from the above-mentioned phenomenological definition, so that a_c is referred to as the *R-matrix (boundary) radius* [16]. $a_c = 100$ fm is used in HHR*. $a_c = 50$ fm [17, 18] is also applicable, and it would lead to a similar result. Although *R-matrix theory* was originally developed for two-body reactions, it has been generalized for a three-body problem, straightforwardly [29].

In *R-matrix expansion* (*e.g.* [16, 22]), linearly-independent scattering waves in the interior region are expanded by

$$\chi_{\alpha\beta}^{l\text{ in}}(k, \rho) = \sum_i A_{i\beta}(k) \chi_{\alpha i}^l(\rho), \quad (58)$$

where α and β are the channel labels. k are hyper-momenta, $k = \sqrt{2m_N E/\hbar^2}$. $A_{i\beta}(k)$ are the coefficients of expansion,

$$\begin{aligned} A_{i\beta}(k) &= \frac{\hbar^2}{2m_N} \frac{1}{\tilde{E}(l_i^\pi) - E} \sum_\gamma \chi_{\gamma i}^l(a_c) \left[H_{K+3/2}^{-\prime}(\eta_\gamma; ka_c) \delta_{\gamma\beta} \right. \\ &\quad \left. - S_{\gamma\beta}^l(E, a_c) H_{K+3/2}^{+\prime}(\eta_\gamma; ka_c) \right]. \end{aligned} \quad (59)$$

$\tilde{E}(l_i^\pi)$ and $\chi_{\alpha i}^l$ are the eigen-energies and eigenfunctions of $\hat{H}_{3\alpha}$, given in Eqs. (47) and (49). $H_{K+3/2}^\pm$ are the incoming ($-$) and outgoing ($+$) Coulomb wavefunctions, defined by

$$H_{K+3/2}^\pm(\eta_\gamma; k\rho) = \tilde{G}_{K+3/2}(\eta_\gamma; k\rho) \pm i\tilde{F}_{K+3/2}(\eta_\gamma; k\rho), \quad (60)$$

where $\tilde{F}_{K+3/2}$ and $\tilde{G}_{K+3/2}$ are the regular and irregular Coulomb wavefunctions, respectively. $S_{\gamma\beta}^l(E, a_c)$ is the three-body S -matrix at $\rho = a_c$,

$$S_{\alpha\beta}^l(E, a_c) = [\mathcal{Z}_{\alpha\beta}^*(E, a_c)]^{-1} \mathcal{Z}_{\alpha\beta}(E, a_c), \quad (61)$$

$$\mathcal{Z}_{\alpha\beta}(E, a_c) = H_{K+3/2}^-(\eta_\alpha; ka_c) \delta_{\alpha\beta} - a_c R_{\alpha\beta}^l(E, a_c) H_{K+3/2}^-(\eta_\beta; ka_c). \quad (62)$$

$R_{\alpha\beta}^l(E, a_c)$ is the R -matrix,

$$R_{\alpha\beta}^l(E, a_c) = \sum_i \frac{\tilde{\gamma}_{\alpha i} \tilde{\gamma}_{\beta i}}{\tilde{E}(l_i^\pi) - E}. \quad (63)$$

$\tilde{\gamma}_{\alpha i}$ are the three-body reduced width amplitudes,

$$\tilde{\gamma}_{\alpha i} = \sqrt{\frac{\hbar^2}{2m_N a_c}} \chi_{\alpha i}^l(a_c). \quad (64)$$

Although the scattering waves are expanded as Eq. (58), additional distortion is brought in by Coulomb couplings in the external region. To take it into consideration, CC equations are numerically solved for the external region. In this calculation, the values of $\chi_{\alpha\beta}^{l\text{ in}}(k, \rho)$ are used as the initial condition. The n_γ independent initial conditions for Eq. (8) make the n_γ linearly-independent solutions. Consequently, the wavefunctions compose the $(n_\gamma \times n_\gamma)$ matrix, expressed as $\chi_{\alpha\beta}^{l\text{ ext}}(k, \rho)$. In §2.5, I describe how to obtain $\chi_{\alpha\beta}^{l\text{ ext}}(k, \rho)$ from $\chi_{\alpha\beta}^{l\text{ in}}(k, \rho)$.

In accordance with the traditional procedure of solving CC equations [15], the numerical solutions satisfying the scattering-boundary condition are obtained from a linear-combination of $\chi_{\alpha\beta}^{l\text{ ext}}(k, \rho)$,

$$\tilde{\chi}_{\gamma\gamma_0}^l(k, \rho) = \sum_{\gamma'} C_{\gamma'\gamma_0}(k) \chi_{\gamma\gamma'}^{l\text{ ext}}(k, \rho), \quad (65)$$

where $C_{\gamma'\gamma_0}$ are the coefficients of expansion. $C_{\gamma'\gamma_0}$ are determined from matching the asymptotic wavefunctions [15, 20],

$$\tilde{\chi}_{\gamma\gamma_0}^l(k, \rho) \rightarrow \frac{i}{2} \left[I_{\gamma, K+3/2}^{(\gamma_0)}(\eta_\gamma; k\rho_m) - \sum_{\gamma'} S_{\gamma'\gamma_0}^l(E) O_{\gamma, K+3/2}^{(\gamma')}(\eta_\gamma; k\rho_m) \right], \quad (66)$$

where ρ_m denotes a matching radius. $S_{\gamma'\gamma_0}^l(E)$ is the S -matrix. $I_{\gamma}^{(\gamma_0)}$ and $O_{\gamma}^{(\gamma')}$ are the incoming and outgoing coupled Coulomb wavefunctions, $I = O^*$,

$$O_{\gamma, K+3/2}^{(\gamma')}(\eta_\gamma; k\rho) = a_{\gamma}^{(\gamma')}(k, \rho) H_{\gamma, K+3/2}^+(\eta_\gamma; k\rho). \quad (67)$$

In the asymptotic region, $a_\gamma^{(\gamma')}$ behaves as $a_\gamma^{(\gamma')} \rightarrow \delta_{\gamma\gamma'}$. However, the wavefunctions even at ρ_m appear to be distorted by Coulomb couplings. Thus, some techniques are required to cope with the long-range behavior of couplings.

The screening technique [17, 18] is one of them. In this method, strength of $V_{\gamma\gamma'}^l$ ($\gamma \neq \gamma'$) is reduced smoothly by a factor,

$$V_{\gamma\gamma'}^l(\rho) \rightarrow V_{\gamma\gamma'}^l(\rho)/\{1 + \exp[(\rho - \rho_{sc})/a_{sc}]\}, \quad (68)$$

where ρ_{sc} and a_{sc} are the screening radius and diffuseness, $\rho_{sc} = 650$ fm and $a_{sc} = 10$ fm. Thus, the interaction matrix is diagonalized at $\rho_m > \rho_{sc}$, and $a_\gamma^{(\gamma')} = \delta_{\gamma\gamma'}$ can be used. The screening technique may be applicable for the triple- α reaction, because the non-diagonal part of coupling potentials is one order of magnitude weaker than the diagonal part. In fact, $a_\gamma^{(\gamma')} = \delta_{\gamma\gamma'}$ could be used without introducing the screening potential, because of $[\mathbf{V}^l(\rho_m) - E\mathbf{1}]$, as demonstrated in §5.1. In the comparison, a ratio of the calculations between screening and no-screening is defined as

$$d_{scrn} = \left| \frac{\sigma_g - \sigma_g^{NS}}{\sigma_g^{NS}} \right| \times 100, \quad (69)$$

where σ_g and σ_g^{NS} represent the calculated cross sections with and without the screening potential.

Using Eq. (58) and $C_{\gamma'\gamma_0}$, I obtain the internal scattering wavefunctions satisfying the asymptotic boundary condition as

$$\begin{aligned} \tilde{\chi}_{\gamma\gamma_0}^{l\ in}(k, \rho) &= \sum_{\gamma'} C_{\gamma'\gamma_0}(k) \chi_{\gamma\gamma'}^{l\ in}(k, \rho) \\ &= \sum_i D_{i\gamma_0}(k) \chi_{\gamma_i}^l(\rho), \end{aligned} \quad (70)$$

$$D_{i\gamma_0}(k) \equiv \sum_{\gamma'} C_{\gamma'\gamma_0}(k) A_{i\gamma'}(k). \quad (71)$$

The three-body continuum states are therefore expanded as

$$\Psi_{lm}^{(+)} = \frac{1}{(k\rho)^{5/2}} \sum_{n\gamma\gamma_0} i^K \left[\sum_i c_{\gamma_i}^n D_{i\gamma_0}(k) \right] \varphi_n^K(\rho) \Phi_{lm}^\gamma(\Omega_5^{(3)}) \Phi_{lm}^{\gamma_0*}(\Omega_5^k), \quad (72)$$

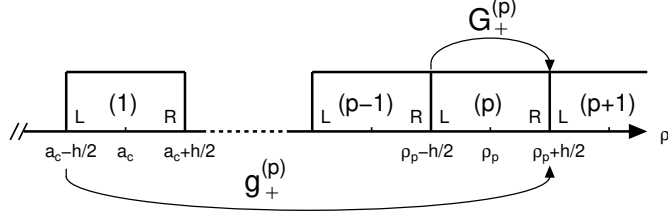


Figure 2: Schematic diagram of sectors in R -matrix propagation.

where Ω_5^k is the angle of \mathbf{k} . In the external region, they are given with the numerical solutions of Eq. (65) as

$$\Psi_{lm}^{(+)} = \frac{1}{(k\rho)^{5/2}} \sum_{\gamma\gamma_0} i^K \tilde{\chi}_{\gamma\gamma_0}^l(k, \rho) \Phi_{lm}^\gamma(\Omega_5^{(3)}) \Phi_{lm}^{\gamma_0*}(\Omega_5^k). \quad (73)$$

2.5. R -matrix propagation

In R -matrix propagation [17, 18], the external region is divided into sectors, as in Fig. 2, and the R -matrix in the $(p-1)$ sector $\mathbf{R}^{(p-1)}$ is propagated to $\mathbf{R}^{(p)}$, as follows:

$$\mathbf{R}^{(p)} = \frac{1}{\rho_R^{(p)}} \left[\mathbf{G}_2^{(p)} (\mathbf{G}_4^{(p)} - \rho_R^{(p-1)} \mathbf{R}^{(p-1)})^{-1} \mathbf{G}_3^{(p)} - \mathbf{G}_1^{(p)} \right], \quad (74)$$

where $p \geq 2$, $\rho_R^{(p-1)} = \rho_p - h/2 = \rho_L^{(p)}$, $\rho_R^{(p)} = \rho_p + h/2$. ρ_p is the center of the p sector. h is a sector size, and it is set to $h = 0.01$ fm in HHR*. The subscript R (L) means the right (left) boundary of the sector. $\mathbf{G}_i^{(p)}$ ($i = 1, 2, 3, 4$) are the propagating matrices, defined by

$$\mathbf{G}_i^{(p)} = \mathcal{T}^{(p)} \Lambda_i^{(p)t} \mathcal{T}^{(p)}. \quad (75)$$

$\mathcal{T}^{(p)}$ is a unitary matrix for diagonalization of a matrix $\mathbf{Q}^{(p)}$,

$${}^t \mathcal{T}^{(p)} \mathbf{Q}^{(p)} \mathcal{T}^{(p)} = \begin{pmatrix} \lambda_1^2(p) & 0 & \dots & 0 \\ 0 & \lambda_2^2(p) & \dots & 0 \\ \vdots & \vdots & \ddots & \vdots \\ 0 & 0 & \dots & \lambda_{n_\gamma}^2(p) \end{pmatrix}, \quad (76)$$

$$Q_{\gamma'\gamma}^{(p)} = \left[\frac{(K+3/2)(K+5/2)}{\rho_p^2} + \epsilon \right] \delta_{\gamma'\gamma} - U_{\gamma'\gamma}^l(\rho_p). \quad (77)$$

$\Lambda_i^{(p)}$ is defined as a diagonal matrix:

$$(\Lambda_1^{(p)})_{\gamma'\gamma} = (\Lambda_4^{(p)})_{\gamma'\gamma} = \delta_{\gamma'\gamma} \begin{cases} -\frac{1}{|\lambda_\gamma(p)| \tanh |h\lambda_\gamma(p)|} & \lambda_\gamma^2(p) > 0 \\ \frac{1}{|\lambda_\gamma(p)| \tan |h\lambda_\gamma(p)|} & \lambda_\gamma^2(p) \leq 0 \end{cases} \quad (78)$$

$$(\Lambda_2^{(p)})_{\gamma'\gamma} = (\Lambda_3^{(p)})_{\gamma'\gamma} = \delta_{\gamma'\gamma} \begin{cases} -\frac{1}{|\lambda_\gamma(p)| \sinh |h\lambda_\gamma(p)|} & \lambda_\gamma^2(p) > 0 \\ \frac{1}{|\lambda_\gamma(p)| \sin |h\lambda_\gamma(p)|} & \lambda_\gamma^2(p) \leq 0 \end{cases} \quad (79)$$

The corresponding wavefunctions and their derivatives at the left boundary of the p sector are calculated from those of the $(p-1)$ sector, as follows:

$$\begin{pmatrix} \chi_L^{(p)} \\ \chi_L^{(p)'} \end{pmatrix} = \mathbf{G}_+^{(p-1)} \begin{pmatrix} \chi_L^{(p-1)} \\ \chi_L^{(p-1)'} \end{pmatrix}, \quad (80)$$

$$\mathbf{G}_+^{(p)} \equiv \begin{pmatrix} \mathbf{G}_1^{(p)} (\mathbf{G}_3^{(p)})^{-1} & [\mathbf{G}_2^{(p)} - \mathbf{G}_1^{(p)} (\mathbf{G}_3^{(p)})^{-1} \mathbf{G}_4^{(p)}] \\ -(\mathbf{G}_3^{(p)})^{-1} & (\mathbf{G}_3^{(p)})^{-1} \mathbf{G}_4^{(p)} \end{pmatrix}. \quad (81)$$

Therefore, $\chi_{\alpha\beta}^{l\ ext}(k, \rho)$ and $d\chi_{\alpha\beta}^{l\ ext}(k, \rho)/d\rho$ are obtained recursively from $\rho = a_c - h/2$. The initial values are given by Eqs. (49) and (58) with Eqs. (25) and (26). To execute stable calculations, quadruple precision is required.

The global propagation matrices $\mathbf{g}_i^{(p)}$ [17, 18] are calculated recursively from $\mathbf{G}_i^{(p)}$, as follows:

$$\mathbf{g}_1^{(p)} = \mathbf{G}_1^{(p)} - \mathbf{G}_2^{(p)} (\mathbf{g}_1^{(p-1)} + \mathbf{G}_4^{(p)})^{-1} \mathbf{G}_3^{(p)}, \quad (82)$$

$$\mathbf{g}_2^{(p)} = \mathbf{G}_2^{(p)} (\mathbf{g}_1^{(p-1)} + \mathbf{G}_4^{(p)})^{-1} \mathbf{g}_2^{(p-1)}, \quad (83)$$

$$\mathbf{g}_3^{(p)} = \mathbf{g}_3^{(p-1)} (\mathbf{g}_1^{(p-1)} + \mathbf{G}_4^{(p)})^{-1} \mathbf{G}_3^{(p)}, \quad (84)$$

$$\mathbf{g}_4^{(p)} = \mathbf{g}_4^{(p-1)} - \mathbf{g}_3^{(p-1)} (\mathbf{g}_1^{(p-1)} + \mathbf{G}_4^{(p)})^{-1} \mathbf{g}_2^{(p-1)}, \quad (85)$$

where $p \geq 2$. The initial values ($p = 1$) are $\mathbf{g}_1^{(1)} = \mathbf{G}_1^{(1)}$, $\mathbf{g}_2^{(1)} = \mathbf{G}_2^{(1)}$, $\mathbf{g}_3^{(1)} = \mathbf{G}_3^{(1)}$, and $\mathbf{g}_4^{(1)} = \mathbf{G}_4^{(1)}$. The global forward propagation matrix is

defined by

$$\mathbf{g}_+^{(p)} \equiv \begin{pmatrix} \mathbf{g}_1^{(p)}(\mathbf{g}_3^{(p)})^{-1} & [\mathbf{g}_2^{(p)} - \mathbf{g}_1^{(p)}(\mathbf{g}_3^{(p)})^{-1}\mathbf{g}_4^{(p)}] \\ -(\mathbf{g}_3^{(p)})^{-1} & (\mathbf{g}_3^{(p)})^{-1}\mathbf{g}_4^{(p)} \end{pmatrix}. \quad (86)$$

The wavefunctions and their derivatives at the right boundary of the p th sector are obtained from those at the left boundary of the first sector, as follows:

$$\begin{pmatrix} \boldsymbol{\chi}_R^{(p)} \\ \boldsymbol{\chi}_R^{(p)'} \end{pmatrix} = \mathbf{g}_+^{(p)} \begin{pmatrix} \boldsymbol{\chi}_L^{(1)} \\ \boldsymbol{\chi}_L^{(1)'} \end{pmatrix}. \quad (87)$$

$\mathbf{g}_+^{(p)}$ is independent of the short-range 3α potentials $V_{3\alpha}^l(\rho)$, and it includes all the effects of the long-range Coulomb couplings. If $\rho_m = \rho_p + h/2$, the wavefunctions and derivatives at ρ_m are given by the single operation at $a_c - h/2$,

$$\begin{aligned} \chi_{\alpha\beta}^{l\ ext}(k, \rho_m) &= \sum_{\gamma} [\mathbf{g}_1^{(p)}(\mathbf{g}_3^{(p)})^{-1}]_{\alpha\gamma} \chi_{\gamma\beta}^{l\ in}(k, a_c - h/2) \\ &+ \sum_{\gamma} [\mathbf{g}_2^{(p)} - \mathbf{g}_1^{(p)}(\mathbf{g}_3^{(p)})^{-1}\mathbf{g}_4^{(p)}]_{\alpha\gamma} \frac{d\chi_{\gamma\beta}^{l\ in}(k, a_c - h/2)}{d\rho}, \quad (88) \\ \frac{d\chi_{\alpha\beta}^{l\ ext}(k, \rho_m)}{d\rho} &= \sum_{\gamma} [-(\mathbf{g}_3^{(p)})^{-1}]_{\alpha\gamma} \chi_{\gamma\beta}^{l\ in}(k, a_c - h/2) \\ &+ \sum_{\gamma} [(\mathbf{g}_3^{(p)})^{-1}\mathbf{g}_4^{(p)}]_{\alpha\gamma} \frac{d\chi_{\gamma\beta}^{l\ in}(k, a_c - h/2)}{d\rho}. \quad (89) \end{aligned}$$

These are the same as those obtained locally from Eq. (80). Therefore, the values calculated from Eqs. (88) and (89) or Eq. (80) are used for the asymptotic matching of Eqs. (65) and (66). The matching radius is $\rho_m = (3000 + 0.005)$ fm [17, 18]. If the screening factor of Eq. (68) is switched on, $\rho_m = (1500 + 0.005)$ fm is also applicable, because the coupling potentials are approximately diagonal at ρ_m .

Likewise, the global backward propagation matrix is defined by

$$\mathbf{g}_-^{(p)} \equiv (\mathbf{g}_+^{(p)})^{-1} = \begin{pmatrix} \mathbf{g}_4^{(p)}(\mathbf{g}_2^{(p)})^{-1} & [\mathbf{g}_4^{(p)}(\mathbf{g}_2^{(p)})^{-1}\mathbf{g}_1^{(p)} - \mathbf{g}_3^{(p)}] \\ (\mathbf{g}_2^{(p)})^{-1} & (\mathbf{g}_2^{(p)})^{-1}\mathbf{g}_1^{(p)} \end{pmatrix}, \quad (90)$$

$$\begin{pmatrix} \boldsymbol{\chi}_L^{(1)} \\ \boldsymbol{\chi}_L^{(1)'} \end{pmatrix} = \mathbf{g}_-^{(p)} \begin{pmatrix} \boldsymbol{\chi}_R^{(p)} \\ \boldsymbol{\chi}_R^{(p)'} \end{pmatrix}. \quad (91)$$

However, $\mathbf{g}_-^{(p)}$ may be devastated by numerical processing at the very low energies. Due to this breakdown, Eq. (91) is not always true in numerical calculations. This global backward propagation is not used in HHR*.

3. Formulae for the triple- α reaction rates

3.1. Transition probability and the reaction rates

The reduced transition strength [16–18] from the 0^+ continuum states to the 2_1^+ bound state in ^{12}C is calculated from

$$\frac{dB(E2; l \rightarrow l')}{dE} = \frac{1}{(2l+1)} \frac{2k^5}{\pi \hbar v} \sum_{m'mq} \int \left| \langle \Psi_{f,l'm'} | \mathcal{M}_{2q}^E | \Psi_{lm}^{(+)} \rangle \right|^2 d\Omega_5^k, \quad (92)$$

where $l = 0$, $l' = 2$, and $f = 1$. q is the projection of multipolarity. \mathcal{M}_{2q}^E denotes the electric quadrupole ($E2$) operator,

$$\begin{aligned} \mathcal{M}_{2q}^E &= 2e[r_1^2 Y_{2q}(\hat{\mathbf{r}}_1) + r_2^2 Y_{2q}(\hat{\mathbf{r}}_2) + r_3^2 Y_{2q}(\hat{\mathbf{r}}_3)] \\ &= \frac{e}{2} \rho^2 [\sin^2 \theta_3 Y_{2q}(\hat{\mathbf{x}}) + \cos^2 \theta_3 Y_{2q}(\hat{\mathbf{y}})], \end{aligned} \quad (93)$$

where \mathbf{r}_i is a distance from the center of mass. Replacing $\Psi_{f,l'm'}$, $\Psi_{lm}^{(+)}$, and \mathcal{M}_{2q}^E with Eqs. (48), (72), (73), and (93), $dB(E2)/dE$ is deduced, as follows:

$$\frac{dB(E2; 0^+ \rightarrow 2_1^+)}{dE} = \frac{5e^2}{2\pi \hbar v} \sum_{\gamma_0} \left| \sum_{\gamma'\gamma} M_{\gamma'\gamma\gamma_0}^{2_1^+ 0^+}(k) (f_{\gamma'\gamma}^x \zeta_x + f_{\gamma'\gamma}^y \zeta_y) \right|^2, \quad (94)$$

where

$$M_{\gamma'\gamma\gamma_0}^{2_1^+ 0^+}(k) = M_{\gamma'\gamma\gamma_0}^{2_1^+ 0^+ \text{Int}}(k) + M_{\gamma'\gamma\gamma_0}^{2_1^+ 0^+ \text{Ext}}(k), \quad (95)$$

$$f_{\gamma'\gamma}^x = \int \phi_{K'}^{l_x l_y}(\theta_3) \sin^4 \theta_3 \cos^2 \theta_3 \phi_K^{l_x l_y}(\theta_3) d\theta_3, \quad (96)$$

$$f_{\gamma'\gamma}^y = \int \phi_{K'}^{l_x l_y}(\theta_3) \sin^2 \theta_3 \cos^4 \theta_3 \phi_K^{l_x l_y}(\theta_3) d\theta_3, \quad (97)$$

$$\zeta_x = \delta_{l_y l'_y} \delta_{l_x l_y} \frac{(-)^{(l'_x+l_x)/2}}{\sqrt{4\pi}} \hat{l}'_x \begin{pmatrix} l'_x & 2 & l_x \\ 0 & 0 & 0 \end{pmatrix}, \quad (98)$$

$$\zeta_y = \delta_{l_x l'_x} \delta_{l_x l_y} \frac{(-)^{(l'_y+l_y)/2}}{\sqrt{4\pi}} \hat{l}'_y \begin{pmatrix} l'_y & 2 & l_y \\ 0 & 0 & 0 \end{pmatrix}. \quad (99)$$

$M_{\gamma'\gamma\gamma_0}^{2_1^+ 0^+ Int}(k)$ and $M_{\gamma'\gamma\gamma_0}^{2_1^+ 0^+ Ext}(k)$ are the interior and external components of transition amplitudes,

$$M_{\gamma'\gamma\gamma_0}^{2_1^+ 0^+ Int}(k) = i^K \sum_i D_{i\gamma_0}(k) \int_0^{a_c} \chi_{\gamma'1}^{2_1^+}(\rho) \chi_{\gamma_i}^{0^+}(\rho) \rho^2 d\rho, \quad (100)$$

$$M_{\gamma'\gamma\gamma_0}^{2_1^+ 0^+ Ext}(k) = i^K \int_{a_c}^{\infty} \chi_{\gamma'1}^{2_1^+}(\rho) \tilde{\chi}_{\gamma_0}^{0^+}(k, \rho) \rho^2 d\rho. \quad (101)$$

The integrals of Eq. (101) converge by $\rho = 200$ fm. The reduced transition probability $B(E2; 0_2^+ \rightarrow 2_1^+)$ is obtained from the integral of Eq. (94) around $E(0_2^+)$, and the γ -decay width of 0_2^+ is given by

$$\Gamma_\gamma(0_2^+) = \frac{4\pi}{75} \left(\frac{\bar{E}_g}{\hbar c} \right)^5 \int_{E(0_2^+) - \Delta\epsilon}^{E(0_2^+) + \Delta\epsilon} \frac{dB(E2; 0_2^+ \rightarrow 2_1^+)}{dE} dE, \quad (102)$$

where \bar{E}_g is γ -ray energy, $\bar{E}_g = E(0_2^+) - E(2_1^+)$. The reduced transition probability from 2_1^+ to the ground state is

$$B(E2; 2_1^+ \rightarrow 0_1^+) = \frac{e^2}{4} \left| \sum_{\gamma'\gamma} M_{\gamma'\gamma}^{2_1^+ 0_1^+} (f_{\gamma'\gamma}^x \zeta_x + f_{\gamma'\gamma}^y \zeta_y) \right|^2, \quad (103)$$

$$M_{\gamma'\gamma}^{2_1^+ 0_1^+} = \int_0^{a_c} \chi_{\gamma'1}^{2_1^+}(\rho) \chi_{\gamma 1}^{0_1^+}(\rho) \rho^2 d\rho. \quad (104)$$

The photo-disintegration of $^{12}\text{C}(2_1^+ \rightarrow 0^+)$ is the inverse reaction of the triple- α process, and its cross sections are given in [16–18] as

$$\sigma_g(E) = \frac{4\pi^3}{75} \left(\frac{E_g}{\hbar c} \right)^3 \frac{1}{5} \frac{dB(E2; 0^+ \rightarrow 2_1^+)}{dE}, \quad (105)$$

where $E_g = E - E(2_1^+)$. The reaction rates of $3\alpha \rightarrow ^{12}\text{C}(2_1^+) + \gamma$ are

$$R_{3\alpha}(E) = N_A^2 \frac{480\pi}{(\mu_{12}\mu_{(12)3})^{3/2}} \frac{\hbar^3}{c^2} \frac{E_g^2}{E^2} \sigma_g(E), \quad (106)$$

where N_A is the Avogadro constant. The energy-averaged reaction rates over the three-body Maxwell-Boltzmann distribution are given by

$$\langle R_{3\alpha} \rangle = \frac{1}{2(k_B T)^3} \int_0^\infty R_{3\alpha}(E) E^2 e^{-E/(k_B T)} dE, \quad (107)$$

where k_B and T are the Boltzmann constant and temperature, respectively.

3.2. Analytic expression of the reaction rates

If a three-body type of S -factors is defined as

$$\begin{aligned} S_{3\alpha}(E) &\equiv E_g^2 \sigma_g(E) \exp\left(\frac{2\pi\eta_0}{\sqrt{E}} + aE\right) \\ &= s_0 (1 + s_1 E + s_2 E^2), \end{aligned} \quad (108)$$

the integral of energy distribution in Eq. (107) is performed with

$$\begin{aligned} E_g^2 \sigma_g(E) e^{-E/k_B T} &= s_0 (1 + s_1 E + s_2 E^2) \exp\left[-\frac{(1 + ak_B T)E}{k_B T} - \frac{2\pi\eta_0}{\sqrt{E}}\right] \\ &= S_{3\alpha}(E) \exp\left[-\left(\frac{E - E_0}{\Delta/2}\right)^2 - \frac{3E_0}{T_a} - \bar{g}\right], \end{aligned} \quad (109)$$

where $T_a = (k_B T)/(1 + ak_B T)$. \bar{g} denotes non-Gaussian components. E_0 and Δ are the Gamow peak energy and energy-window for the direct triple- α process,

$$E_0 = (\pi\eta_0 T_a)^{2/3}, \quad (110)$$

$$\Delta = (4/\sqrt{3}) (\pi\eta_0)^{1/3} T_a^{5/6}. \quad (111)$$

s_0 , s_1 , s_2 , η_0 , and a are determined from the calculated $E_g^2 \sigma_g(E)$. With this expansion, the non-resonant reaction rates are analytically expressed as

$$\langle R_{3\alpha} \rangle_{NR} = N_A^2 \frac{45\pi\sqrt{\pi} \hbar^3}{2m_N^3 c^2} \frac{(\pi\eta_0)^{1/3}}{(k_B T)^{13/6} (1 + ak_B T)^{5/6}} \tilde{S}(T_a) \exp\left[-\frac{3(\pi\eta_0)^{2/3}}{T_a^{1/3}}\right], \quad (112)$$

$$\tilde{S}(T_a) \approx s_0 \left[\left(1 + \frac{5T_a}{36E_0}\right) + s_1 E_0 \left(1 + \frac{35T_a}{36E_0}\right) + s_2 E_0^2 \left(1 + \frac{89T_a}{36E_0}\right) \right]. \quad (113)$$

Table 1: Parameters of $\alpha+\alpha$ potentials in Eq. (116). The values of AB are taken from [10, 18, 30]. CD is based on [31–34]. The values of CD are determined so as to reproduce the resonant energy and width of ${}^8\text{Be}(0_1^+)$, and experimental elastic phase shifts [35–38]. The values of J_v , defined by Eq. (117), are also listed as net strength of potentials.

	$V_{c0}(\text{MeV})$	$V_{c2}(\text{MeV})$	$r_c(\text{fm})$	$V_0(\text{MeV})$	$r_v(\text{fm})$	$J_v(\text{MeV fm}^3)$
AB	125.0	20.0	1.53	-30.18	2.85	243
CD	295.45	197.8	1.57	-118.7	2.16	416

The significant term at low temperatures may be represented by

$$\langle R_{3\alpha} \rangle_{NR} \approx \frac{\tilde{b}_0}{T_9^{13/6}} \exp\left(-\frac{\tilde{b}_1}{T_9^{1/3}}\right). \quad (114)$$

This simplified version is used for REACLIB translation. \tilde{b}_0 and \tilde{b}_1 are adjusted so as to minimize a difference from the expression of Eq. (112).

The resonant contribution in Eq. (107) is analytically expressed as

$$\begin{aligned} \langle R_{3\alpha} \rangle_R &= \frac{9\sqrt{3}\pi^3}{4} \frac{N_A^2 \hbar^5}{m_N^3} \frac{\Gamma_\gamma(0_2^+)}{(k_B T)^3} \exp\left(-\frac{E(0_2^+)}{k_B T}\right) \\ &\approx 7.605 \times 10^{-9} \frac{\Gamma_\gamma(0_2^+)}{T_9^3} \exp\left(-\frac{11.605 E(0_2^+)}{T_9}\right), \end{aligned} \quad (115)$$

where $\Gamma_\gamma(0_2^+)$ is in meV, and $E(0_2^+)$ is in MeV. $\langle R_{3\alpha} \rangle_R$ is given in the unit of $\text{cm}^6 \text{mol}^{-2} \text{s}^{-1}$.

4. Interaction potentials and the lowest three states in ${}^{12}\text{C}$

In this section, I describe the interaction potentials for $\alpha+\alpha$ and 3α , and I examine the generated states to discuss the available range of 3α potentials.

4.1. $\alpha+\alpha$ potentials

Two types of interaction potentials between $\alpha+\alpha$ are adopted in Eq. (37). One is the so-called modified Ali-Bodmer (AB) potential [10, 11, 14, 18, 30]. The other is a deep potential based on the double folding (DF) model [31, 32]. The repulsive core potentials are introduced so as to satisfy the Pauli principle

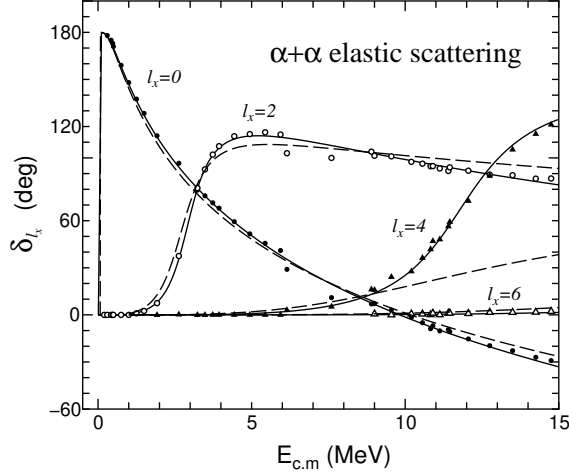


Figure 3: Phase shifts of $\alpha+\alpha$ elastic scattering. The solid and dashed curves are the results calculated from the CD and AB potentials, respectively. The experimental data are taken from [35–38].

[33]. This phase-equivalent potential is referred to as the core plus deep (CD) potential in the present article. AB and CD are given in

$$V_N^{l_{x_i}}(\bar{x}_i) = V_{cl_{x_i}} \hat{\mathbf{P}}_{l_{x_i}} e^{-(\bar{x}_i/r_c)^2} + V_0 e^{-(\bar{x}_i/r_v)^2}, \quad (116)$$

for $l_{x_i} = \text{even}$. $\hat{\mathbf{P}}_{l_{x_i}}$ are Pauli exclusion operators. V_{c0} , V_{c2} , V_0 , r_c , and r_v are listed in Table 1. For CD, the parameters are determined so as to reproduce the resonant energy and width of ${}^8\text{Be}(0_1^+)$, and the experimental phase shifts of elastic scattering [35–38]. The calculated phase shifts are compared with the experimental data in Fig. 3. The solid and dashed curves are the results obtained from the CD and AB potentials, respectively. As shown in Fig. 3, AB cannot reproduce the phase shifts of $l_x = 4$. As a value of net strength, the volume integral of potentials per nucleon pair J_v is defined by

$$J_v = \frac{\pi^{3/2} |V_0| r_v^3}{16}. \quad (117)$$

From the values of J_v in Table 1, AB is found to be shallower than CD. J_v of CD seems to be consistent with that of the studies in [32, 39, 40].

AB and CD are compared with the DF potential [32, 39] in Fig. 4(A). The dashed, solid, and dotted curves are the AB, CD, and DF potentials,

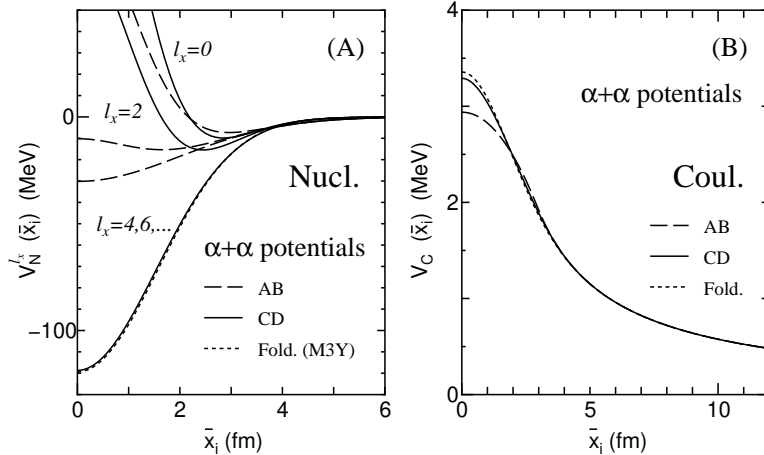


Figure 4: $\alpha+\alpha$ potentials: (A) Nuclear and (B) Coulomb parts. The solid and dashed curves are the CD and AB potentials, respectively. The dotted curves are calculated from the DF procedure [32, 39] with M3Y [34] and Coulomb interaction.

respectively. The DF potential is calculated from

$$V_F(\bar{x}_i) = \int \rho_\alpha(r_j)\rho_\alpha(r_k)v_{nn}(r_k + \bar{x}_i - r_j)dr_jdr_k, \quad (118)$$

where r_j and r_k are the internal coordinates of ${}^4\text{He}$. v_{nn} is M3Y effective nucleon-nucleon interaction [34] with single-nucleon exchange. $\rho_\alpha(r)$ is $(0s)^4$ shell model density of ${}^4\text{He}$, given by $\rho_\alpha(r) = 0.41251 \exp[-(r/1.2031)^2]$. The range is determined so as to reproduce the experimental charge radius, 1.6768 fm [41]. The rms radius of this density is $\langle r_\alpha^2 \rangle^{1/2} = 1.4735$ fm, and it is also used in Eq. (55). From Fig. 4(A), the CD potential for $l_x \geq 4$ (even parity) is confirmed to be identical to the DF potential.

Coulomb potentials $V_C(\bar{x}_i)$ are compared in Fig. 4(B). The styles of curves are the same as those in Fig. 4(A). The Coulomb potential for AB is calculated from the point + uniform charge distribution of the radius 2.94 fm [18]. For CD, it is calculated with two uniform charge spheres [42]. The radii are set to 2.1 fm so as to make an equivalent potential to the folded one. The Coulomb potentials are independent of the parity and l_{x_i} .

The calculated resonant energy and width for ${}^8\text{Be}(0_1^+)$ from CD are $E_R = 91.3$ keV and $\Gamma = 5.79$ eV. These are obtained from an R -matrix fit to the calculated s -wave phase shifts, and they are comparable with the

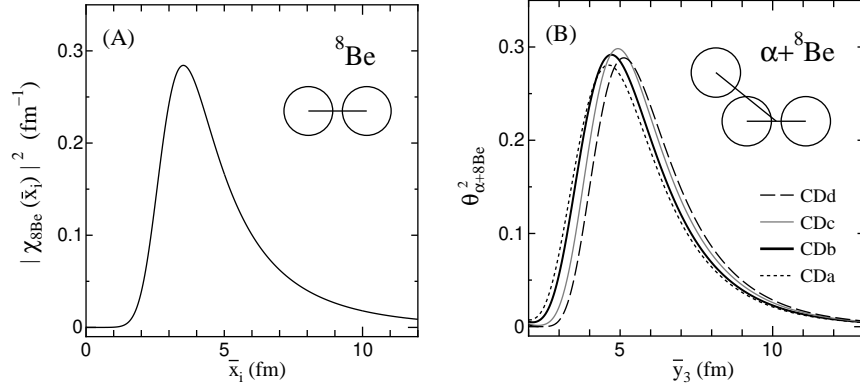


Figure 5: (A) Density distribution of relative motion between $\alpha+\alpha$ in ${}^8\text{Be}(0_1^+)$, obtained from the CD potential. The most probable relative distance is found to be 3.52 fm. The resonance energy $E_R = 91.3$ keV and width $\Gamma = 5.79$ eV are derived from the s -wave phase shifts. (B) Dimensionless reduced width for $\alpha+{}^8\text{Be}$ in ${}^{12}\text{C}(0_2^+)$, defined in Eq. (54). The dotted, bold solid, thin solid, and dashed curves are obtained from CDa, CDb, CDc, and CDd, respectively. The dilute structure is developed as $r_{3\alpha}$ increases.

experimental values [43]: $E_R = 91.8$ keV and $\Gamma = 5.57 \pm 0.25$ eV. The corresponding wavefunction of relative motion between $\alpha+\alpha$ is depicted in Fig. 5(A), $\chi_{8\text{Be}} = \bar{x}_i \Psi_{8\text{Be}}$. From the solid curve, the most probable relative distance is expected to be 3.52 fm. This wavefunction is used in Eq. (52) to estimate $\theta_{\alpha+8\text{Be}}^2$, which is displayed in Fig. 5(B).

CD is similar to AB(D) used in CMF. However, AB(D) makes $E_R = 95.1$ keV and $\Gamma = 8.32$ eV for ${}^8\text{Be}(0_1^+)$ [11]. They do not seem to be better than those of CD. The nucleon density distribution in DF is calculated from the intrinsic wavefunction of α -particle. This means that the internal structure of ${}^4\text{He}$ is included in the $\alpha+\alpha$ potential. To take account of the microscopic aspect, I adopt CD as an equivalent local potential, updating the parameters to make a better reproduction of the experimental data. In addition, AB used in ACF is assumed to be independent of l_x , *i.e.*, ACF cannot even reproduce the $l_x = 2$ phase shifts of $\alpha+\alpha$.

4.2. 3α potentials

The 3α potentials in Eq. (36) are defined, as follows:

$$V_{3\alpha}^l(\rho) = v_{3\alpha,l} \exp \left[- \left(\frac{\rho}{r_{3\alpha}} \right)^2 \right]. \quad (119)$$

Table 2: Variations in the quantities for the generated states to the range of 3α potentials. $r_{3\alpha}$ and $v_{3\alpha,l}$ are defined in Eq. (119). $E(l_i^\pi)$ is the energy of states with l^π . q_{mix} is a mixing ratio of $\alpha+{}^8\text{Be}$ clustering in 0_2^+ . The rms radius of 0_2^+ , defined as Eq. (55), is also listed. \mathcal{N}^2 is defined in Eq. (57).

		CDa	CDb	CDc	CDd	AB
$r_{3\alpha}$	(fm)	3.46	4.0	5.0	6.0	6.0
$v_{3\alpha,0}$	(MeV)	-154.55	-86.965	-37.15	-19.447	-20.145
$v_{3\alpha,2}$	(MeV)	-82.06	-44.49	-21.14	-13.43	-16.36
$E(0_2^+)$	(MeV)	0.3794	0.3796	0.3796	0.3795	0.3795
$E(2_1^+)$	(MeV)	-2.837	-2.836	-2.836	-2.836	-2.838
$E(0_1^+)$	(MeV)	-7.726	-8.005	-7.213	-6.152	-5.187
q_{mix}		0.52	0.56	0.63	0.65	0.61
$R_{\text{rms}}(0_2^+)$	(fm)	3.35	3.41	3.52	3.59	3.75
\mathcal{N}^2		0.784	0.928	1.054	1.863	1.637

$v_{3\alpha,l}$ and $r_{3\alpha}$ are adjusted so as to minimize a difference from the experimental energies of 0_2^+ and 2_1^+ in ${}^{12}\text{C}$ [10, 11, 14, 18]. The resultant values and calculated $E(l_i^\pi)$ are listed in Table 2. Including the 3α potential, AB is basically the same as the potentials in [18]. For CD, I examine $r_{3\alpha} = 3.46, 4.0, 5.0,$ and 6.0 fm. In the present article, they are referred to as CDa, CDb, CDc, and CDd, respectively, along with the $\alpha+\alpha$ potential. CDa and CDb may resemble $\text{AB(D)}+\Delta(3.45)$ and $\text{AB(D)}+\Delta(3.9)$, recommended in [13]. CDd and AB seem to generate the slightly high $E(0_1^+)$.

4.3. Density distribution functions of 0_2^+ and 2_1^+ in ${}^{12}\text{C}$

Figure 6(A) shows the density distribution function of 0_2^+ obtained from CDb. This color contour plot seems similar to that from HHR [18], CMF [12], and [44]. Two conspicuous peaks are located on $(\bar{x}_3, \bar{y}_3) = \text{a}(3.4 \text{ fm}, 4.4 \text{ fm})$ and $\text{b}(2.6 \text{ fm}, 2.1 \text{ fm})$, and a plateau is found at long \bar{x}_3 and short \bar{y}_3 . A weak islet also appears at $(\bar{x}_3, \bar{y}_3) = \text{d}(3.5 \text{ fm}, 0.4 \text{ fm})$. The peak (a) has an $\alpha+{}^8\text{Be}$ configuration, because the relative distance \bar{x}_3 in ${}^{12}\text{C}(0_2^+)$ is close to that in ${}^8\text{Be}(0_1^+)$. The peak (b) corresponds to a configuration of equilateral triangle with sizes approximately 2.6 fm. The plateau (c) is obtuse triangle, and the height at (c) is half of (a), $\mathcal{P}_{0_2^+}(c) = \mathcal{P}_{0_2^+}(a)/2$ [12]. (d) is almost linear alignment. Because (c) is geometrically associated with (a), the 0_2^+ state is confirmed to have dual aspects: (a) dilute $\alpha+{}^8\text{Be}$ and (b) spatially-shrunk structure corresponding to quantum liquid [45, 46]. In addition, it is

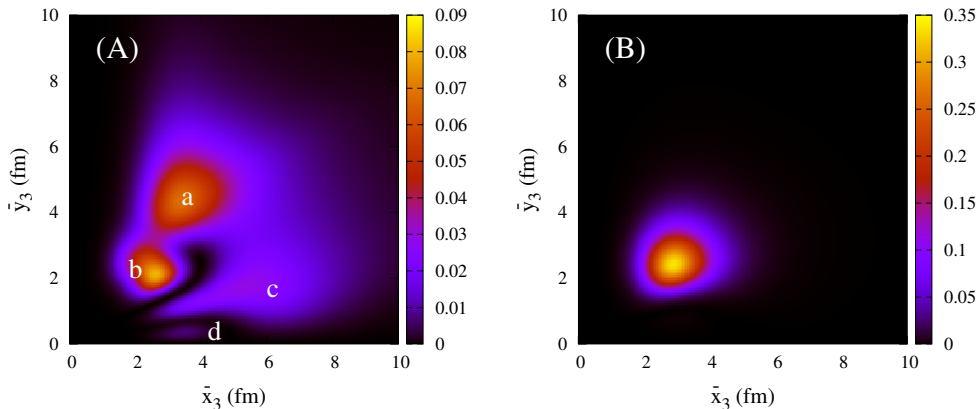


Figure 6: Density distribution functions of (A) 0_2^+ and (B) 2_1^+ , defined in Eq. (51), calculated from HHR* with CDb. The horizontal and vertical axes are \bar{x}_3 and \bar{y}_3 in Fig. 1. The results of HHR* seem to be similar to those of HHR [18], CMF [12], and [44].

confirmed to decay dominantly via $\alpha+^8\text{Be}$ because of the penetrability.

The similar density distributions of 0_2^+ can be obtained with CDa, CDc, CDd, and AB. However, the peak values are slightly varied. To assess the differences, I define a mixing ratio of (a) dilute $\alpha+^8\text{Be}$ to (b) spatial-shrunk structure, $q_{mix} \equiv 1 - \mathcal{P}_{0_2^+}(b)/[1.5 \times \mathcal{P}_{0_2^+}(a) + \mathcal{P}_{0_2^+}(b)]$, as a guide. From q_{mix} in Table 2, the dilute structure is found to develop as $r_{3\alpha}$ increases in CD. Especially, CDc and CDd may be preferable from 61% [45] clustering in 0_2^+ . This feature can be also seen in $\theta_{\alpha+^8\text{Be}}^2$ of Fig. 5(B). As $r_{3\alpha}$ increases, the peak of $\theta_{\alpha+^8\text{Be}}^2$ is shifted to large \bar{y}_3 , and α -particle probability increases for $\bar{y}_3 > 5$ fm. $R_{\text{rms}}(0_2^+)$ also becomes larger, as listed in Table 2. The differences between CDd and AB may stem from the $\alpha+\alpha$ potential.

For 2_1^+ , single peak is found in the density distribution function obtained from CDb (Fig. 6(B)). This corresponds to a spatial-shrunk configuration of equilateral triangle with sizes approximately 2.8 fm. The similar contour plots can be obtained with CDa, CDc, CDd, and AB. \mathcal{N}^2 of Eq. (57), obtained within a factor of 2 (Table 2), are consistent with those in HHR, CMF, and ACF. Especially, CDb and CDc seem to be preferable. The ground state also has the same configuration as 2_1^+ .

Considering the variations to $r_{3\alpha}$ discussed above, I calculate the recommended values from CDb, and I show the uncertainties of the results by using CDa and CDc in §5.

Table 3: Comparison in $E(l_i^\pi)$, $R_{\text{rms}}(l_i^\pi)$, $B(E2)$, $M(E0)$, and $\Gamma(0_2^+)$. The values of HHR* are the present results with CDb, and they appear to be concordant with the results of HHR [18], CMF [11], ACF [14], and the experimental data [27].

		HHR*	HHR [18]	CMF [11]	ACF [14]	Exp. [27]
$E(0_2^+)$	(MeV)	0.3796	0.380	0.378	0.379	0.379
$E(2_1^+)$	(MeV)	-2.836	-2.875	-2.83	-2.836	-2.835
$E(0_1^+)$	(MeV)	-8.005		-7.789	-9.242	-7.275
$R_{\text{rms}}(0_2^+)$	(fm)	3.41		3.43	4.00	
$R_{\text{rms}}(2_1^+)$	(fm)	2.39	2.459		2.40	
$R_{\text{rms}}(0_1^+)$	(fm)	2.36			2.30	2.35–2.48
$B(E2; 0_2^+ \rightarrow 2_1^+)$	($e^2\text{fm}^4$)	15.2		8.7	34.6	13.8
$B(E2; 2_1^+ \rightarrow 0_1^+)$	($e^2\text{fm}^4$)	8.00			12.4	7.76
$M(E0; 0_2^+ \rightarrow 0_1^+)$	($e\text{fm}^2$)	5.54			6.44	5.48
$\Gamma(0_2^+)$	(eV)	7.1		6.9	15.8	9.3

In Table 3, $E(l_i^\pi)$, $R_{\text{rms}}(l_i^\pi)$, $B(E2)$, $M(E0)$, and $\Gamma(0_2^+)$ of CDb are compared with those of [11, 14, 18, 27]. The present results appear to be concordant with the previous values. $R_{\text{rms}}(0_2^+)$ is longer than $R_{\text{rms}}(0_1^+)$, whereas $R_{\text{rms}}(2_1^+)$ is similar to $R_{\text{rms}}(0_1^+)$. The derived monopole matrix element of Eq. (56) is $5.54 e\text{fm}^2$. The calculated charge radius of $^{12}\text{C}(0_1^+)$ is 2.49 fm, comparable to the experimental value 2.48 fm [27]. The $\alpha+^8\text{Be}$ width, given by Eq. (53), is 2.37 eV at $\bar{y}_3 = 6$ fm. Thus, the calculated α -decay width is obtained as 7.1 eV, and it appears to be consistent with [27].

5. Results: Triple- α reaction rates

In this section, I discuss the calculated results of the triple- α reaction rates, after illustrating the photo-disintegration of $^{12}\text{C}(2_1^+ \rightarrow 0^+)$ and the S -factor. At the same time, I discuss the difference between adiabatic and non-adiabatic approaches. The derived rates are expressed in an analytic form, and they are provided in a tabular form. They are also converted into REACLIB format. I finally discuss an update to the evaluated reaction rates.

5.1. Comparison between photo-disintegration cross sections

The photo-disintegration cross sections of $^{12}\text{C}(2_1^+ \rightarrow 0^+)$, calculated from HHR* with CDb, are shown by the solid curve in Fig. 7. A prominent narrow

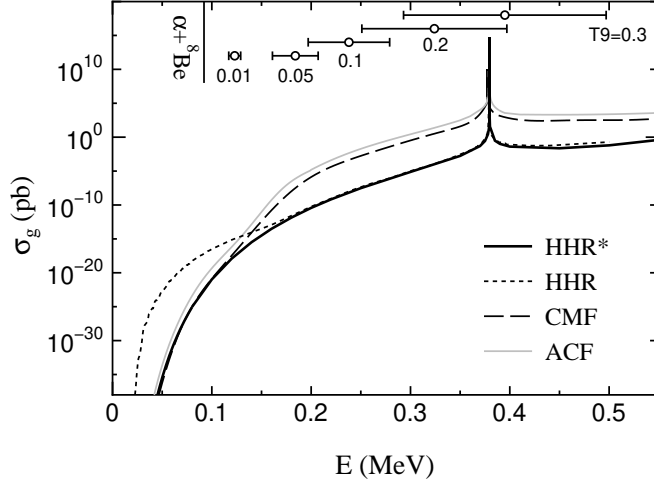


Figure 7: Cross sections for photo-disintegration of $^{12}\text{C}(2_1^+ \rightarrow 0^+)$. The solid curve is the result obtained from HHR* with CD δ . The dotted, dashed, and gray curves are taken from HHR [18], CMF [11], and ACF [14], respectively. The Gamow peak energy [4] and energy-window [4] for $\alpha+^8\text{Be}$ at $T_9 = 0.01, 0.05, 0.1, 0.2,$ and 0.3 are displayed by the open circles and horizontal bars as a guide of the energy range for the sequential process.

resonance of 0_2^+ is found at $E \approx 0.379$ MeV, and the smoothly varying non-resonant cross sections are obtained at off-resonant energies. For $0.15 \leq E \leq 0.35$ MeV, I find $\sigma_g = 10^{-15} - 10^{-3}$ pb order of magnitude. This result appears to be almost identical to HHR [18] shown by the dotted curve. Below $E = 0.15$ MeV, σ_g of HHR* seems similar to that of CMF (dashed curve) and ACF (gray curve). On the other hand, the present results at off-resonant energies above $E = 0.15$ MeV are 10^{-4} order of magnitude smaller than the values predicted by CMF and ACF. CMF has been developed in the three-body bound states and p+d reactions. The internal motion of ^8Be in break-up channels is assumed to be localized within a certain range [11]. For ACF, the adiabatic potential, generated separably with a fixed hyperradius, is characterized by $\alpha+^8\text{Be}$ at short radii and by 3α at large radii, and their σ_g for $E \geq 0.13$ MeV has been interpreted as a part of the 0_2^+ resonance [14]. Judging from their theoretical approaches, most of the differences above $E = 0.15$ MeV seem to stem from the internal adiabatic feature. The adiabatic approach to ^8Be continuum states makes the assumed long resonant tail of 0_2^+ , leading to the sequential decay process at off-resonant energies, and it might have enhanced the photo-disintegration cross sections unexpectedly.

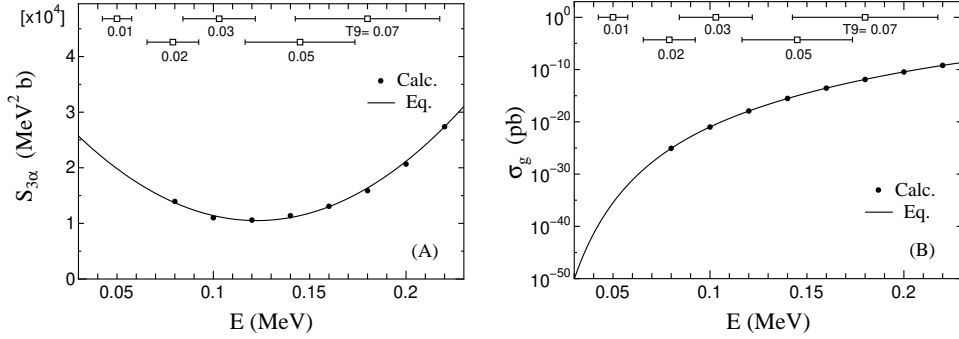


Figure 8: (A) S -factors and (B) cross sections for photo-disintegration of $^{12}\text{C}(2_1^+ \rightarrow 0^+)$. The solid circles are the calculated values from HHR* with CDb. The solid curves are (A) $S_{3\alpha}(E) = 3.717 \times 10^4 \cdot (1 - 11.71E + 47.79E^2)$ $\text{MeV}^2 \text{ b}$ and (B) $\sigma_g(E) = S_{3\alpha}(E)(E + 2.836)^{-2} \exp(-26.125/\sqrt{E} - 5E)$ b. The open squares and horizontal bars are the Gamow peak energy and energy-window at the respective temperatures for the direct triple- α process, defined in Eqs. (110) and (111).

The enhancement of [18] for $E < 0.15$ MeV seems to be caused by the redundant global backward propagation of Eq. (91) and the difference in the Coulomb potentials of Eq. (38).

The Gamow peak energy and energy-window for $\alpha + {}^8\text{Be}$ are given by $E_{\alpha^8\text{Be}} = 0.677T_9^{2/3} + 0.092$ MeV [4] and $\Delta_{\alpha^8\text{Be}} = 0.558T_9^{5/6}$ [4], and they are shown by the open circles and horizontal bars in Fig. 7. From the difference above $E = 0.15$ MeV, the reaction rate of HHR* at $T_9 = 0.05$ is expected to be 10^{-4} order of magnitude smaller than that of CMF and ACF.

To examine the long-range Coulomb couplings, I also execute the calculations without the screening potential. The differences, defined as Eq. (69), are $d_{scrn} = 0.75\%$, 0.34% , 0.31% , 0.30% , and 0.07% at $E = 0.2, 0.3, 0.3796, 0.4,$ and 0.5 MeV. I, therefore, find that the differences are less than 1% at the energies corresponding to helium burning temperatures, and that the Coulomb couplings seem to be negligible for $\rho > 650$ fm in practice.

The calculated σ_g below $E = 0.2$ MeV appear to be expressed with $S_{3\alpha}$. The solid circles in Fig. 8(A) are the calculated values of HHR* with CDb, and the solid curve is $S_{3\alpha}(E) = 3.717 \times 10^4 \cdot (1 - 11.71E + 47.79E^2)$ $\text{MeV}^2 \text{ b}$. Compared with σ_g in Fig. 8(B), the energy dependence of $S_{3\alpha}$ is quite weak. The open squares and horizontal bars are the Gamow peak energy and energy-window for 3α , defined in Eqs. (110) and (111). In the present article, the

Table 4: Coefficients in the S -factors of Eq. (108). The resonant energy and γ width of 0_2^+ are also listed. The triple- α reaction rates for 0^+ are obtained from these quantities with Eqs. (112), (113), and (115). The recommended rates are obtained from CDb.

	s_0 (MeV ² b)	s_1 (MeV ⁻¹)	s_2 (MeV ⁻²)	η_0 (MeV ^{1/2})	a (MeV ⁻¹)	$E(0_2^+)$ (MeV)	$\Gamma_\gamma(0_2^+)$ (meV)
CDa	1.416×10^4	-11.18	43.87	4.068	5.0	0.3794	3.9
CDb	3.717×10^4	-11.71	47.79	4.158	5.0	0.3796	3.9
CDc	3.075×10^4	-11.71	48.83	4.152	5.0	0.3796	3.9
CDd	3.525×10^4	-11.60	48.40	4.129	5.0	0.3795	3.9
AB	9.166×10^4	-11.66	48.08	4.125	5.0	0.3795	3.9

reaction rates below $T_9 \approx 0.02$ are generated from the extrapolated $S_{3\alpha}$, assuming that $S_{3\alpha}$ has weak variation to E . The cross sections from CDa, CDc, CDd, and AB are also expressed with $S_{3\alpha}$ similarly well. The resultant coefficients are summarized in Table 4. From these quantities, the triple- α reaction rates for 0^+ are given with Eqs. (112), (113), and (115).

5.2. Triple- α reaction rates

The resulting reaction rates are shown in Fig. 9: (A) in the unit of $\text{cm}^6 \text{mol}^{-2} \text{s}^{-1}$ and (B) in ratio to NACRE. The bold solid curves are the result obtained from CDb, and they are expressed as

$$\begin{aligned}
 \langle R_{3\alpha} \rangle = & \left[\frac{229.7}{T_9^{13/6}(1+bT_9)^{5/6}} + \frac{2.5}{T_9^{11/6}(1+bT_9)^{7/6}} - \frac{2911.}{T_9^{3/2}(1+bT_9)^{3/2}} \right. \\
 & \left. - \frac{225.}{T_9^{7/6}(1+bT_9)^{11/6}} + \frac{1.285 \times 10^4}{T_9^{5/6}(1+bT_9)^{13/6}} + \frac{2.53 \times 10^3}{T_9^{1/2}(1+bT_9)^{5/2}} \right] \\
 & \cdot \exp \left[-\frac{37.673}{T_9^{1/3}}(1+bT_9)^{1/3} \right] + \frac{2.966 \times 10^{-8}}{T_9^3} \exp \left(-\frac{4.4053}{T_9} \right),
 \end{aligned} \tag{120}$$

where $b = 0.431$. As shown in this figure, the derived rates are found to be consistent with NACRE at helium burning temperatures (horizontal bars). Especially, the rates are approximately proportional to T_9^{41} at $T_9 = 0.1$, as well as NACRE, so that they are expected to make a red-giant consistently in the late stage of stellar evolution.

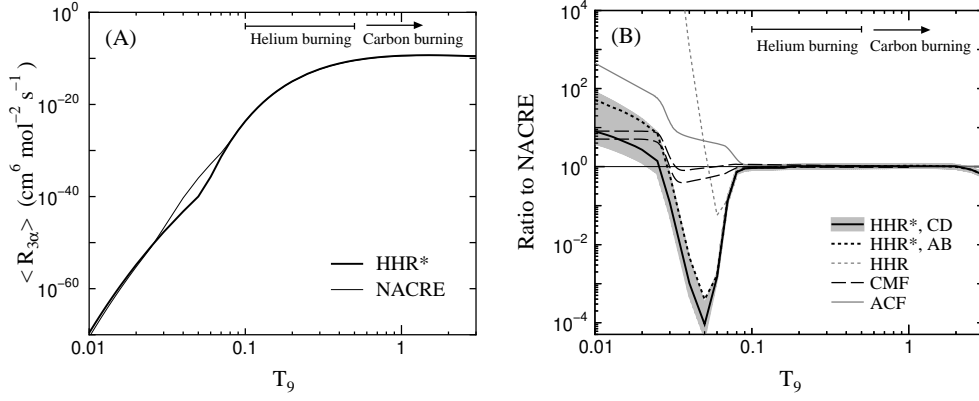


Figure 9: Triple- α reaction rates (A) in the unit of $\text{cm}^6 \text{mol}^{-2} \text{s}^{-1}$ and (B) in ratio to NACRE. The bold solid and bold dotted curves are the result obtained from HHR* with CD and AB. The dotted, dashed, and gray curves are taken from HHR [18], CMF [11], and ACF [14], respectively. The thin solid curve is the NACRE reaction rates [4]. The horizontal bars are the range of helium burning temperatures. The gray shade represents the uncertainties of the present rates.

On the other hand, the present result is also found to be reduced by about 10^{-4} at $T_9 = 0.05$. The dashed and gray curves are taken from CMF [11] and ACF [14]. As shown in Fig. 7, the present rate is much smaller than that of CMF and ACF at $T_9 = 0.05$, because σ_g is reduced from theirs at $E = 0.18$ MeV. Due to the strong influence of 0_2^+ , the large difference in σ_g above $E = 0.20$ MeV does not make a large deviation in the rates above $T_9 = 0.08$. The similar reduction can be found in the rates from AB, shown by the bold dotted curve. From a comparison between the bold solid and bold dotted curves, I confirm that the reduction at $T_9 = 0.05$ does not stem from the adopted $\alpha + \alpha$ potentials.

Table 5: Triple- α reaction rates by HHR*. The rates are given in the unit of $\text{cm}^6\text{mol}^{-2}\text{s}^{-1}$. The recommended rates $\langle R_{3\alpha} \rangle$ are obtained from CDb, and they are analytically expressed with Eq. (120). $\langle R_{3\alpha} \rangle_L$ and $\langle R_{3\alpha} \rangle_U$ are the lower and upper limits, respectively. The ratios to CF88 [7] and NACRE [4] are also listed for reference.

T_9	$\langle R_{3\alpha} \rangle_L$	$\langle R_{3\alpha} \rangle$	$\langle R_{3\alpha} \rangle_U$	10^x	CF88	NACRE	T_9	$\langle R_{3\alpha} \rangle_L$	$\langle R_{3\alpha} \rangle$	$\langle R_{3\alpha} \rangle_U$	10^x	CF88	NACRE
0.010	1.15	2.33	23.2	-70	87.	7.9	0.15	1.40	1.55	1.73	-18	1.0	0.97
0.011	2.08	4.23	39.1	-68	79.	7.1	0.16	7.22	7.99	8.92	-18	1.0	0.97
0.012	2.05	4.20	36.2	-66	72.	6.4	0.18	1.08	1.20	1.33	-16	1.0	0.98
0.013	1.24	2.54	20.6	-64	66.	5.7	0.20	9.09	10.1	11.2	-16	1.0	0.99
0.014	4.98	10.2	78.7	-63	60.	5.1	0.25	3.81	4.22	4.69	-14	1.1	1.0
0.015	1.42	2.92	21.4	-61	54.	4.6	0.30	4.16	4.61	5.11	-13	1.1	1.0
0.016	3.03	6.24	43.7	-60	48.	4.1	0.35	2.13	2.36	2.62	-12	1.1	1.0
0.018	6.73	13.9	89.9	-58	35.	3.3	0.40	6.89	7.64	8.45	-12	1.1	1.0
0.020	7.00	14.5	87.3	-56	24.	2.7	0.45	1.64	1.82	2.02	-11	1.1	1.0
0.025	7.50	15.5	81.0	-52	5.7	1.4	0.50	3.19	3.54	3.91	-11	1.1	1.0
0.03	8.80	18.2	84.2	-49	0.29	0.12	0.60	8.01	8.89	9.82	-11	1.1	1.0
0.04	2.71	5.55	21.1	-44	1.9×10^{-3}	1.0×10^{-3}	0.70	1.44	1.60	1.76	-10	1.1	1.0
0.05	4.55	9.43	30.1	-41	1.6×10^{-4}	9.1×10^{-5}	0.80	2.12	2.35	2.59	-10	1.1	1.0
0.06	1.65	1.81	2.08	-36	2.6×10^{-3}	1.5×10^{-3}	0.90	2.74	3.05	3.36	-10	1.1	1.0
0.07	3.66	4.03	4.59	-32	0.23	0.13	1.0	3.26	3.62	3.99	-10	1.1	1.0
0.08	6.39	7.05	7.98	-29	0.92	0.73	1.25	4.03	4.48	4.93	-10	1.1	1.0
0.09	2.04	2.25	2.54	-26	1.0	0.89	1.5	4.20	4.66	5.13	-10	1.1	1.0
0.10	1.98	2.19	2.47	-24	1.0	0.92	1.75	4.02	4.47	4.92	-10	1.1	1.0
0.11	8.17	9.02	10.1	-23	1.0	0.94	2.0	3.69	4.10	4.51	-10	1.1	0.99
0.12	1.77	1.96	2.19	-21	1.0	0.94	2.5	2.94	3.26	3.59	-10	1.1	0.83
0.13	2.34	2.59	2.90	-20	1.0	0.95	3.0	2.28	2.54	2.79	-10	1.1	0.61
0.14	2.11	2.33	2.61	-19	1.0	0.96							

Table 6: Coefficients of expansion in REACLIB format, obtained from HHR* with CDb. The reaction rates are defined as Eq. (121). The maximum deviation from Eq. (120) is also listed.

i	a_{i0}	a_{i1}	a_{i2}	a_{i3}	a_{i4}	a_{i5}	a_{i6}	(%)
1	2.4379	0.	-37.219	0.	-1.4	0.	-13/6	14
2	-17.333	-4.4053	0.	0.	0.	0.	-3.	n/a

The uncertainties of the rates are shown by the gray shade in Fig. 9(B). The upper and lower limits are defined as $\langle R_{3\alpha} \rangle_U = 1.1 \times \langle R_{3\alpha} \rangle_a$ and $\langle R_{3\alpha} \rangle_L = 0.9 \times \langle R_{3\alpha} \rangle_c$ for $T_9 \geq 0.06$, including the experimental uncertainty of $\Gamma_\gamma(0_2^+)$. For $T_9 \leq 0.05$, they are assumed as $\langle R_{3\alpha} \rangle_U = 2 \times \langle R_{3\alpha} \rangle_a$ and $\langle R_{3\alpha} \rangle_L = \langle R_{3\alpha} \rangle_c/2$. $\langle R_{3\alpha} \rangle_a$ and $\langle R_{3\alpha} \rangle_c$ are the rates obtained from CDa and CDc, respectively. The numerical values of the resultant rates are listed in Table 5.

5.3. Translation into REACLIB

The recommended rates of HHR*, shown in the previous subsection, are converted into REACLIB format [23]:

$$\begin{aligned} \langle R_{3\alpha} \rangle = & \sum_i \exp(a_{i0} + a_{i1}/T_9 + a_{i2}/T_9^{1/3} + a_{i3}T_9^{1/3} + a_{i4}T_9 \\ & + a_{i5}T_9^{5/3} + a_{i6} \ln(T_9)). \end{aligned} \quad (121)$$

a_{ij} are the coefficients of expansion. Equation (114) is adopted for the non-resonant component, and a_{i4} is used for high temperatures. The resultant a_{ij} are listed in Table 6. The maximum deviation from Eq. (120) is also listed. The converted rates are displayed in Fig. 10(A). The dashed ($i = 1$) and solid ($i = 2$) curves are the non-resonant and resonant components, respectively. In REACLIB [23], two data sets, labeled with CF88 [7] and FY05 [47], are compiled as the triple- α reaction rates. They are also shown in Figs. 10(B) and 10(C). Both of them consist of three components. The dashed and dotted curves contribute below $T_9 = 0.07$ as the non-resonant components, and the solid curves represent the resonant component. Compared with CF88 and FY05, HHR* does not have a component of the dotted curve.

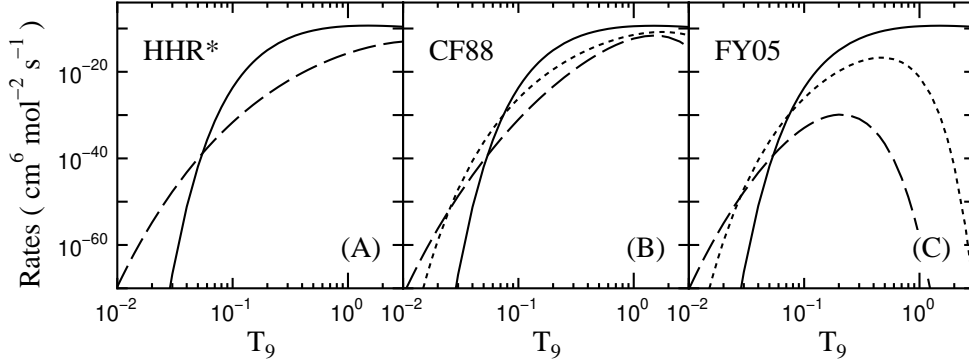


Figure 10: Comparison with the triple- α reaction rates in REACLIB [23]: (A) HHR*, this work, (B) CF88, and (C) FY05. HHR* consists of two components, whereas CF88 and FY05 consist of three components. The solid and dashed curves represent the resonant and non-resonant components, respectively. The dotted curves seem to originate from the assumed bound ${}^8\text{Be}$ in CF88 and FY05, and they are interpreted as the non-resonant sequential process between $\alpha+{}^8\text{Be}$. HHR* does not have such a component. The statistically generated ${}^8\text{Be}$ is broken-up immediately by the third α -particle at $T_9 \approx 0.05$.

To understand why the REACLIB rates have three components, let me recall the method used in NACRE. In [4], the triple- α reaction rates are given as

$$\begin{aligned}
\langle R_{3\alpha} \rangle &= \frac{24\hbar N_A^2}{\pi(\mu_{12}\mu_{(12)3})^{1/2}(k_B T)^3} \\
&\cdot \int_0^\infty dE_1 \int_0^\infty dE_2 \frac{\sigma_{\alpha\alpha}(E_1)\sigma_{\alpha^8\text{Be}}(E_2; E_1)}{\Gamma_\alpha({}^8\text{Be}, E_1)} E_1 E_2 \exp\left(-\frac{E_1 + E_2}{k_B T}\right) \\
&= \int_{E_{R1}-\Delta\epsilon_1}^{E_{R1}+\Delta\epsilon_1} \int_{E_{R2}-\Delta\epsilon_2}^{E_{R2}+\Delta\epsilon_2} \bigcirc dE_1 dE_2 + \int_{E_{R1}-\Delta\epsilon_1}^{E_{R1}+\Delta\epsilon_1} \int_{\text{other}} \bigcirc dE_1 dE_2 \\
&+ \int_{\text{other}} \int_{E_{R2}-\Delta\epsilon_2}^{E_{R2}+\Delta\epsilon_2} \bigcirc dE_1 dE_2 + \int_{\text{other}} \int_{\text{other}} \bigcirc dE_1 dE_2 \\
&\equiv (\langle R_{3\alpha} \rangle_{DR} + \langle R_{3\alpha} \rangle_{{}^8\text{Be}} + \langle R_{3\alpha} \rangle_{{}^{12}\text{C}} + \langle R_{3\alpha} \rangle_{NRs})/100. \tag{122}
\end{aligned}$$

$\Gamma_\alpha({}^8\text{Be}, E_1)$ and $\sigma_{\alpha\alpha}$ are the energy-dependent α -width of ${}^8\text{Be}$ and elastic cross sections between $\alpha+\alpha$, respectively, and they give ${}^8\text{Be}$ formation probability. $\sigma_{\alpha^8\text{Be}}$ is the radiative capture cross sections of $\alpha+{}^8\text{Be}$. E_1 is the center-of-mass energy of relative motion between $\alpha+\alpha$, and E_2 is the energy

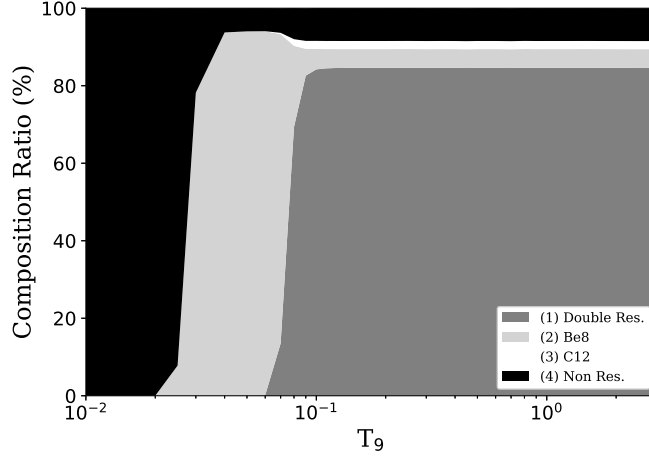


Figure 11: Composition ratio of the triple- α reaction rates for 0^+ in NACRE [4]. The rates are calculated from Eq. (122) with the adopted experimental resonant energies and widths in [4]. The dense and black areas are $\langle R_{3\alpha} \rangle_{DR} / \langle R_{3\alpha} \rangle$ and $\langle R_{3\alpha} \rangle_{NRs} / \langle R_{3\alpha} \rangle$, respectively. The gray area represents $\langle R_{3\alpha} \rangle_{sBe} / \langle R_{3\alpha} \rangle$, the non-resonant sequential process between $\alpha + {}^8\text{Be}$. The white area is $\langle R_{3\alpha} \rangle_{12C} / \langle R_{3\alpha} \rangle$, and it is small in the entire region. The standard reaction rates are found to generally consist of three components.

between $\alpha + {}^8\text{Be}$. In the first line of Eq. (122), the integral of E_1 can be divided into two: the ${}^8\text{Be}$ resonance energy region $E_{R1} \pm \Delta\epsilon_1 = 92.08 \pm 0.03$ keV and the other. Likewise, the integral of E_2 can be divided into $E_{R2} \pm \Delta\epsilon_2 = 287.7 \pm 0.05$ keV and the other. Consequently, the NACRE rates are expressed with four components in the second line, and they are expressed as (1) double resonances of ${}^8\text{Be}$ and ${}^{12}\text{C}$, $\langle R_{3\alpha} \rangle_{DR}$, (2) ${}^8\text{Be}$ resonance, $\langle R_{3\alpha} \rangle_{sBe}$, (3) ${}^{12}\text{C}$ resonance, $\langle R_{3\alpha} \rangle_{12C}$, and (4) non-resonant contributions, $\langle R_{3\alpha} \rangle_{NRs}$, in the third line. These composition ratios are shown in Fig. 11. $\langle R_{3\alpha} \rangle_{DR} / \langle R_{3\alpha} \rangle$ and $\langle R_{3\alpha} \rangle_{NRs} / \langle R_{3\alpha} \rangle$ are shown by the dense and black areas, respectively. $\langle R_{3\alpha} \rangle_{DR}$ accounts for over 80% above $T_9 = 0.09$, and $\langle R_{3\alpha} \rangle_{NRs}$ dominates the rates for $T_9 \leq 0.025$. $\langle R_{3\alpha} \rangle_{sBe} / \langle R_{3\alpha} \rangle$ is shown by the gray area, and it is found to dominate the rates for $0.03 \leq T_9 \leq 0.07$. $\langle R_{3\alpha} \rangle_{12C} / \langle R_{3\alpha} \rangle$, shown by the white area, is small over the entire region. The rates from 2_2^+ [48] and 3_1^- [49] of ${}^{12}\text{C}$ are small below $T_9 = 3$. Therefore, the standard reaction rates below $T_9 = 3$ are found to generally consist of three components.

If they are classified into the reaction process, $\langle R_{3\alpha} \rangle_{DR}$ means the sequential process via two narrow resonances, and $\langle R_{3\alpha} \rangle_{NRs}$ reminds us of the

direct triple- α process. The component of $\langle R_{3\alpha} \rangle_{^8\text{Be}}$ is interpreted as the non-resonant sequential process between $\alpha + ^8\text{Be}$. However, this term may not seem to be realistic, because ^8Be is unbound. In other words, the dotted curves in Fig. 10 seem to originate from the assumed ^8Be in CF88 and FY05. From the present non-adiabatic calculation, the statistically generated ^8Be is found to be broken-up immediately by the third α -particle before its lifetime at $T_9 \approx 0.05$. My calculated results, therefore, indicate that the non-resonant sequential process could be at least eliminated by hand, to update the reaction rates in NACRE and REACLIB.

6. Summary

The present article has discussed the direct triple- α process and derived reaction rates by using the non-adiabatic Faddeev HHR* expansion method. First, I have reviewed this theory and setup. The main differences between HHR and HHR* seem to stem from the matching procedure for asymptotic wavefunctions (§2.4), and Coulomb potentials in the asymptotic region (§2.2), in addition to the adopted basis functions. In §3.2, I have introduced the three-body S -factors, and I have deduced the formula of reaction rates, attaching the resonant component.

In §4, I have described the adopted potentials and the generated states of ^8Be and ^{12}C , and I have examined the available range $r_{3\alpha}$ of 3α potentials. The CD potential, based on the DF model, reproduces the experimental phase shifts of $\alpha + \alpha$ elastic scattering and the $^8\text{Be}(0_1^+)$ resonance. In contrast, the nuclear potential of AB is shallower than that of CD, and it cannot reproduce the $l_x = 4$ phase shifts. The density distribution function of 0_2^+ in ^{12}C is confirmed to have dual aspects: dilute $\alpha + ^8\text{Be}$ and spatially-shrunk structure. The mixing ratio of this dilute clustering depends on $r_{3\alpha}$. Whereas $r_{3\alpha} = 3.46$ fm (CDa) and 4.0 fm (CDb) are recommended by CMF and ACF, $r_{3\alpha} = 5.0$ fm (CDc) and 6.0 fm (CDd) seem to be preferable from [45, 46]. In addition, I have confirmed that the 2_1^+ state has a spatially-shrunk configuration of equilateral triangle with the almost same size as the ground state. The resultant rms radii of 0_2^+ and 2_1^+ seem to be consistent with those from HHR, CMF, and ACF. The calculated charge radius of 0_1^+ , $B(E2; 0_2^+ \rightarrow 2_1^+)$, $B(E2; 2_1^+ \rightarrow 0_1^+)$, $M(E0; 0_2^+ \rightarrow 0_1^+)$, and $\Gamma(0_2^+)$ are also concordant with the experimental values.

I have discussed the calculated reaction rates in §5, illustrating the calculated photo-disintegration cross sections of $^{12}\text{C}(2_1^+ \rightarrow 0^+)$ and the cor-

responding S -factors. At the same time, I have discussed the difference between adiabatic and non-adiabatic calculations. The calculated photo-disintegration at off-resonant energies is estimated to be in $10^{-15} - 10^{-3}$ pico-barn order of cross sections σ_g for $0.15 \leq E \leq 0.35$ MeV. This is far below the values predicted by ACF and CMF. In spite of the large difference, the derived reaction rates are concordant with the NACRE rates for $0.08 \leq T_9 \leq 3$. The difference in σ_g below $E = 0.20$ MeV can be seen in the rates for $T_9 \leq 0.07$. In comparison with the calculations, I have found that the triple- α reaction rates are reduced by about 10^{-4} at $T_9 = 0.05$, because of the accurate description for ${}^8\text{Be}$ break-up. In addition to the analytic form, the present rates are provided in the tabular form. The recommended rates are made from CDb. The uncertainties of the rates have been estimated by examining sensitivity to 3α potentials. The upper and lower limits are estimated from CDa and CDc within a factor of 2 for $T_9 \leq 0.05$. The rates obtained from AB are similar to those from CD. Thus, I have confirmed that the reduction at $T_9 = 0.05$ does not stem from the adopted $\alpha+\alpha$ potentials. To examine the long-range Coulomb couplings, I have also demonstrated the calculations without screening, and I have found that the Coulomb coupling effects are negligible for $\rho > 650$ fm at the energies corresponding to helium burning temperatures.

Finally, I have converted the derived rates into REACLIB format, and I have shown that the present rates do not have the component of the non-resonant sequential process between $\alpha+{}^8\text{Be}$. My calculated results, therefore, suggest that this component could be at least eliminated by hand, to update the rates in NACRE and REACLIB.

Acknowledgments

I thank M. Arnould and Y. Sakuragi for drawing my attention to this subject and for their hospitality during my stay at Université Libre de Bruxelles and Osaka City University. This research did not receive any specific grant from funding agencies in the public, commercial, or not-for-profit sectors.

References

- [1] F. Hoyle, *Astrophys. J. Suppl. Ser.* 1 (1954) 121. doi:10.1086/190005.
- [2] E.E. Salpeter, *Astrophys. J.* 115 (1952) 326. doi:10.1086/145546.

- [3] M. Katsuma, JPS Conf. Proc. 31 (2020) 011060; Springer Proc. in Phys. 219 (2019) 389; Phys. Rev. C 78 (2008) 034606.
doi:10.7566/JPSCP.31.011060; doi:10.1007/978-3-030-13876-9_72;
doi:10.1103/PhysRevC.78.034606.
- [4] C. Angulo, M. Arnould, M. Rayet, et al., Nucl. Phys. A 656 (1999) 3.
doi:10.1016/S0375-9474(99)00030-5.
- [5] R. Smith, Tz. Kokalova, C. Wheldon, et al., Phys. Rev. Lett. 119 (2017) 132502. doi:10.1103/PhysRevLett.119.132502.
- [6] D. Dell'Aquila, I. Lombardo, G. Verde, et al., Phys. Rev. Lett. 119 (2017) 132501. doi:10.1103/PhysRevLett.119.132501.
- [7] G.R. Caughlan, W.A. Fowler, Atom. Data Nucl. Data Tables 40 (1988) 283. doi:10.1016/0092-640X(88)90009-5.
- [8] K. Nomoto, F.-K. Thielemann, S. Miyaji, Astron. Astrophys. 149 (1985) 239. 1985A&A...149..239N.
- [9] K. Langanke, M. Wiescher, F.-K. Thielemann, Z. Phys. A 324 (1986) 147. doi:10.1007/BF01325126.
- [10] D.V. Fedorov, A.S. Jensen, Phys. Lett. B 389 (1996) 631.
doi:10.1016/S0370-2693(96)80001-3.
- [11] S. Ishikawa, Phys. Rev. C 87 (2013) 055804.
doi:10.1103/PhysRevC.87.055804.
- [12] S. Ishikawa, Phys. Rev. C 90 (2014) 061604; Few-Body Syst. 65 (2024) 50. doi:10.1103/PhysRevC.90.061604; doi:10.1007/s00601-024-01922-4.
- [13] S. Ishikawa, Phys. Rev. C 94 (2016) 061603.
doi:10.1103/PhysRevC.94.061603.
- [14] H. Suno, Y. Suzuki, P. Descouvemont, Phys. Rev. C 94 (2016) 054607.
doi:10.1103/PhysRevC.94.054607.
- [15] G.R. Satchler, Direct Nuclear Reactions, Oxford University Press, New York, 1983.

- [16] I.J. Thompson, F.M. Nunes, Nuclear Reactions for Astrophysics, Cambridge University Press, New York, 2009.
- [17] N.B. Nguyen, F.M. Nunes, I.J. Thompson, E.F. Brown, Phys. Rev. Lett. 109 (2012) 141101. doi:10.1103/PhysRevLett.109.141101.
- [18] N.B. Nguyen, F.M. Nunes, I.J. Thompson, Phys. Rev. C 87 (2013) 054615; N.B. Nguyen, Ph.D. dissertation, Michigan State University (2013). doi:10.1103/PhysRevC.87.054615; doi:10.25335/M55F37.
- [19] A.M. Lane, R.G. Thomas, Rev. Mod. Phys. 30 (1958) 257. doi:10.1103/RevModPhys.30.257.
- [20] M. Katsuma, Communications in Physics vol. 32 no. 4S (2022) 585; arXiv:2302.03844. doi:10.48550/arXiv.2302.03844.
- [21] P. Descouvemont, J. Phys. G 37 (2010) 64010. doi:10.1088/0954-3899/37/6/064010.
- [22] P. Descouvemont, Theoretical Models for Nuclear Astrophysics, Nova Science Publishers, New York, 2003.
- [23] JINA REACLIB Database, [https://reaclib.jinaweb.org/he4\(aa,g\)c12](https://reaclib.jinaweb.org/he4(aa,g)c12).
- [24] M. Katsuma, Y. Sakuragi, S. Okabe, Y. Kondō, Prog. Theor. Phys. 107 (2002) 377. doi:10.1143/PTP.107.377.
- [25] J. Raynal, J. Revai, Il Nuovo Cimento A 68 (1970) 612. doi:10.1007/BF02756127.
- [26] V. Vasilevsky, F. Arickx, W. Vanroose, and J. Broeckhove, Phys. Rev. C85, 034318 (2012); V. Vasilevsky, A.V. Nesterov, F. Arickx, and J. Broeckhove, Phys. Rev. C63, 034606 (2001). doi:10.1103/PhysRevC.85.034318; doi:10.1103/PhysRevC.63.034606.
- [27] J.H. Kelley, J.E. Purcell, C.G. Sheu, Nucl. Phys. A 968 (2017) 71. doi:10.1016/j.nuclphysa.2017.07.015.
- [28] P. Descouvemont, D. Baye, Rep. Prog. Phys. 73 (2010) 036301. doi:10.1088/0034-4885/73/3/036301.

- [29] I.J. Thompson, B.V. Danilin, V.D. Efros, J.S. Vaagen, J.M. Bang, M.V. Zhukov, Phys. Rev. C 61 (2000) 024318.
doi:10.1103/PhysRevC.61.024318.
- [30] S. Ali, A.R. Bodmer, Nucl. Phys. 80 (1966) 99.
doi:10.1016/0029-5582(66)90829-7.
- [31] B. Buck, H. Friedrich, C. Wheatley, Nucl. Phys. A 275 (1977) 246.
doi:10.1016/0375-9474(77)90287-1.
- [32] G.R. Satchler, W.G. Love, Phys. Rep. 55 (1979) 183.
doi:10.1016/0370-1573(79)90081-4.
- [33] D. Baye, Phys. Rev. Lett. 58 (1987) 2738.
doi:10.1103/PhysRevLett.58.2738.
- [34] G. Bertsch, J. Borysowicz, H. McManus, W.G. Love, Nucl. Phys. A 284 (1977) 399. doi:10.1016/0375-9474(77)90392-X.
- [35] N.P. Heydenburg, G.M. Temmer, Phys. Rev. 104 (1956) 123.
doi:10.1103/PhysRev.104.123.
- [36] R. Nilson, W.K. Jentschke, G.R. Briggs, et al., Phys. Rev. 109 (1958) 850. doi:10.1103/PhysRev.109.850.
- [37] T.A. Tombrello, L.S. Senhouse, Phys. Rev. 129 (1963) 2252.
doi:10.1103/PhysRev.129.2252.
- [38] W.S. Chien, R.E. Brown, Phys. Rev. C 10 (1974) 1767.
doi:10.1103/PhysRevC.10.1767.
- [39] M.E. Brandan, G.R. Satchler, Phys. Rep. 285 (1997) 143.
doi:10.1016/S0370-1573(96)00048-8.
- [40] M. Katsuma, J Phys. G 40 (2013) 025107.
doi:10.1088/0954-3899/40/2/025107.
- [41] H. de Vries, C.W. de Jager, C. de Vries, Atom. Data Nucl. Data Tables 36 (1987) 495. doi:10.1016/0092-640X(87)90013-1.
- [42] R.M. Devries, M.R. Clover, Nucl. Phys. A 243 (1975) 528.
doi:10.1016/0375-9474(75)90294-8.

- [43] D.R. Tilley, J.H. Kelley, J.L. Godwin, et al., Nucl. Phys. A 745 (2004) 155. doi:10.1016/j.nuclphysa.2004.09.059.
- [44] H. Moriya, W. Horiuchi, J. Casal, L. Fortunato, Few-Body Syst. 62 (2021) 46. doi:10.1007/s00601-021-01631-2.
- [45] T. Otsuka, T. Abe, T. Yoshida, et al., Nature Communications 13 (2022) 2234. doi:10.1038/s41467-022-29582-0.
- [46] A. Tohsaki, H. Horiuchi, P. Schuck, G. Röpke, Phys. Rev. Lett. 87 (2001) 192501. doi:10.1103/PhysRevLett.87.192501.
- [47] H.O.U. Fynbo, C.Aa. Diget, U.C. Bergmann, et al., Nature 433 (2005) 136. doi:10.1038/nature03219.
- [48] W.R. Zimmerman, M.W. Ahmed, B. Bromberger, et al., Phys. Rev. Lett. 110 (2013) 152502. doi:10.1103/PhysRevLett.110.152502.
- [49] M. Tsumura, T. Kawabata, Y. Takahashi, et al., Phys. Lett. B 817 (2021) 136283. doi:10.1016/j.physletb.2021.136283.